Supplementary Information for

Ammonia Mobilizes Cobalt Ions in Zeolites to Form Dimeric Active Sites for Ethane Activation

Yongwoo Kim[1, 5, †], Asanka Wijerathne[2,†], Mohan J. Shankar[2], Jieun Lee[1], Enrico Tusini[3], Adam Hoffman[3], Simon R. Bare[3], Xue Chen[4], Christopher Paolucci[2*], David W. Flaherty[1*]

[1]School of Chemical & Biomolecular Engineering, Georgia Institute of Technology; Atlanta, Georgia, 30332, United States

[2]Department of Chemical Engineering, University of Virginia; Charlottesville, Virginia, 22903, United States

[3]SSRL, SLAC National Accelerator Laboratory, Menlo Park, California 94025, United States

[4]Dow Industrial Solutions, The Dow Chemical Company, Freeport, Texas, 77566, United States

[5]School of Chemical, Biological & Battery Engineering, Gachon University, Gyeonggi-do 13120, Republic of Korea

[†]These authors contributed equally to this work

*Corresponding authors. Email: cp9wx@virginia.edu, dflaherty3@gatech.edu

Table of Contents

Computational Methods

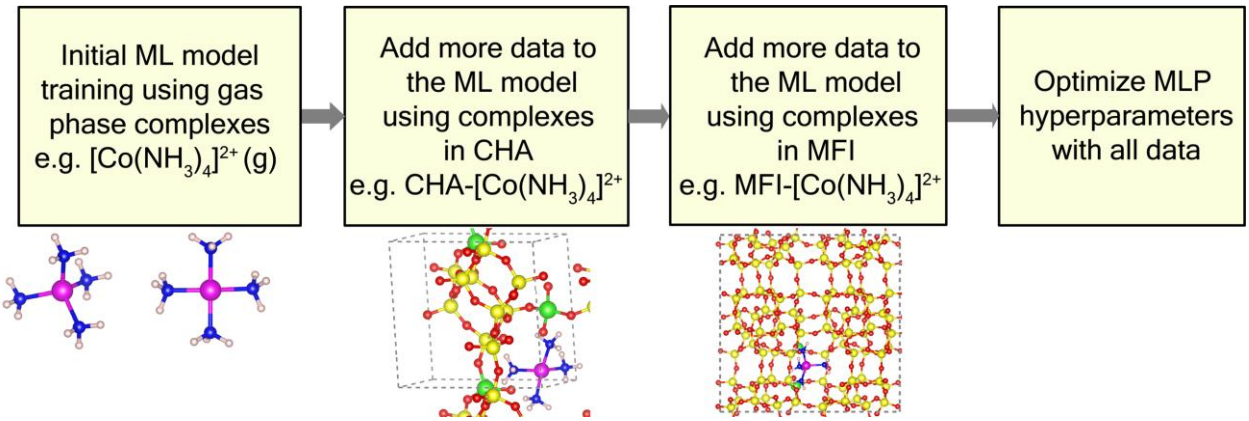

Supplementary Scheme 1. Workflow of FLARE MLP training using a sequential approach. Unit cells of CHA and MFI are shown in grey dashed lines.

Supplementary Table 1. Number of images (DFT calculations) used from each system (clusters, CHA, MFI) for training of the $[Co(H_2O)_n]^{2+}$ MLP.

Structure	Encapsulation environment	Number of training images
$[\mathbf{Co(H_2O)_6}]^{2+}$ octahedreal	Vacuum	105
$[\mathbf{Co(H_2O)_4}]^{2+}$ square planar	Vacuum	49
$[\mathbf{Co(H_2O)_4}]^{2+}$ tetrahedral	Vacuum	46
$[\mathbf{Co(H_2O)_4}]^{2+}$ square planar	CHA	52
$[\mathbf{Co(H_2O)_4}]^{2+}$ tetrahedral	MFI	26

Supplementary Table 2. Number of images (DFT calculations) used from each system (clusters, CHA, MFI) for training of the $[Co(NH_3)_m(H_2O)_n]^{2+}$ MLP.

Structure	Encapsulation environment	Number of training images
$[\mathbf{Co(NH_3)_6}]^{2+}$ octahedral	Vacuum	156
$[\mathbf{Co(NH_3)_4}]^{2+}$ square planar	Vacuum	64
$[\mathbf{Co(NH_3)_4(H_2O)_2}]^{2+}$ octahedral	Vacuum	79
$[\mathbf{Co(NH_3)_2(H_2O)_2}]^{2+}$ square planar/ tetrahedral	Vacuum	88
$[\mathbf{Co(NH_3)_4}]^{2+}$ tetrahedral	Vacuum	37
$[\mathbf{Co(NH_3)_4}]^{2+}$ square planar	CHA	52
$[\mathbf{Co(NH_3)_4}]^{2+}$ tetrahedral	MFI	32
$[\mathbf{Co(NH_3)_4(H_2O)_2}]^{2+}$ octahedral, 773 K	MFI	46

Supplementary Table 3. Number of images (DFT calculations) used from each system (clusters, CHA, MFI) for training of the $[Co(NH_3)_4\text{-}O_2\text{-}Co(NH_3)_4]^{4+}$/$[Co(NH_3)_4\text{-}O_2]^{2+}$ MLP.

Structure	Encapsulation environment	Number of training images
$[(NH_3)_4Co-O_2-Co(NH_3)_4]^{4+}$	Vacuum	144
$[(NH_3)_4Co=O_2]^{2+}$ peroxo	Vacuum	39
$[(NH_3)_4Co-O_2]^{2+}$ superoxo	Vacuum	21
$[(NH_3)_4Co-O]^{2+}$ oxo	Vacuum	45
$[(NH_3)_4Co-O_2-Co(NH_3)_4]^{4+}$	MFI	44
$[(NH_3)_4Co=O_2]^{2+}$ peroxo	MFI	14
$[(NH_3)_4Co-O_2-Co(NH_3)_4]^{4+}$, 773 K	MFI	58

Validation of $[Co(H_2O)_n]^{2+}$ MLPs

Force and energy errors for training each MLP are reported in Supplementary Figs. 1, 4 and 7. Validation data (DFT calculations for structures not included in the training data) for the three MLPs are reported in Supplementary Figs. 2-3, 5-6, and 8-9, and the initial structures used for training each potential with a sample MLP training script are included in the supplementary information files. The trained GPs are larger than 200 GB, therefore, we only include sample training scripts in the SM Data File to generate the MLPs as necessary for future studies. All three MLPs show acceptable errors for testing data, with mean absolute errors (MAE) for energies of 0.6-0.9 meV/atom and force MAEs of 0.11-0.19 eV/Å. These errors are similar to errors reported for other zeolite MLPs [1, 2].

Validation for MLP

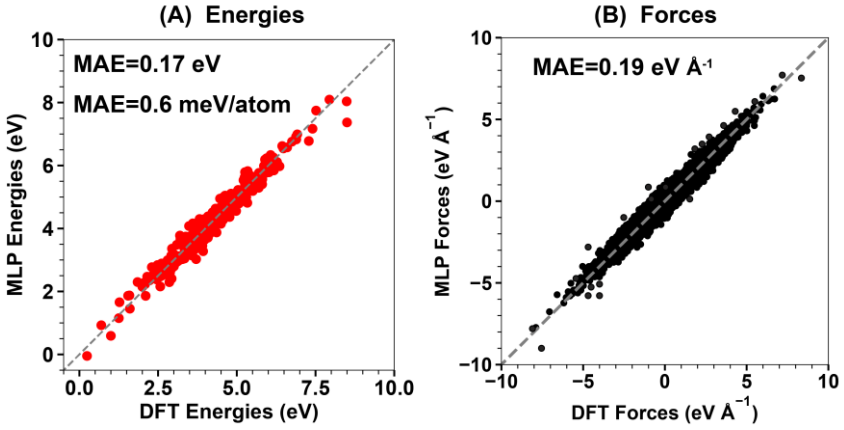

Supplementary Fig. 1. (A) Energies and (B) Forces predicted using the FLARE model during on-the-fly training (278 structures).

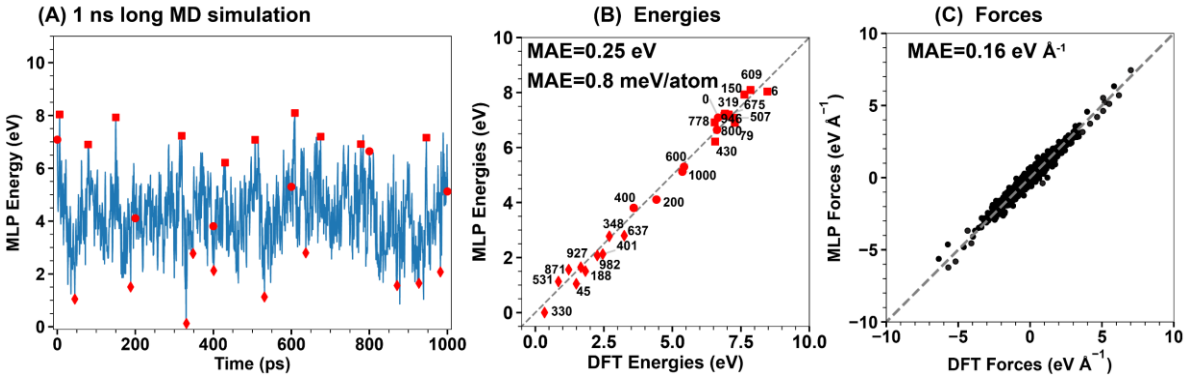

Supplementary Fig. 2. Validation of the FLARE MLP using DFT. Parity plots of (B) Energies and (C) Forces estimated from the FLARE potential vs DFT for $[Co(H_2O)_4]^{2+}$ in the 4Al config. 4. MD simulation settings are T = 648 K (Nosé–Hoover thermostat), timestep = 0.5 fs and total simulation time of 1 ns. For the model training, only the 4Al config. 1 in MFI was used with other structures (clusters and CHA, Supplementary Scheme 1). Diamond, square, and circle symbols are local minima, local maxima, and structures that are 200 ps apart, respectively while simulation time (in ps) is shown in B for each structure obtained from the MD trajectory.

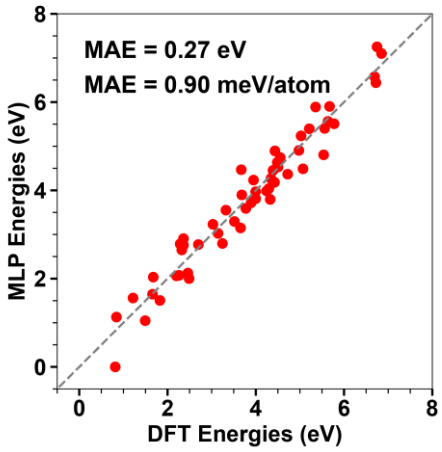

Supplementary Fig. 3. FLARE MLP and DFT energies of the 50 local minima structures identified for $[Co(H_2O)_4]^{2+}$ in five different 4Al configurations shown in Fig. 3A. The energies are relative to the lowest MLP energy structure (E=0).

Validation for $[Co(NH_3)_m(H_2O)_n]^{2+}$ MLP

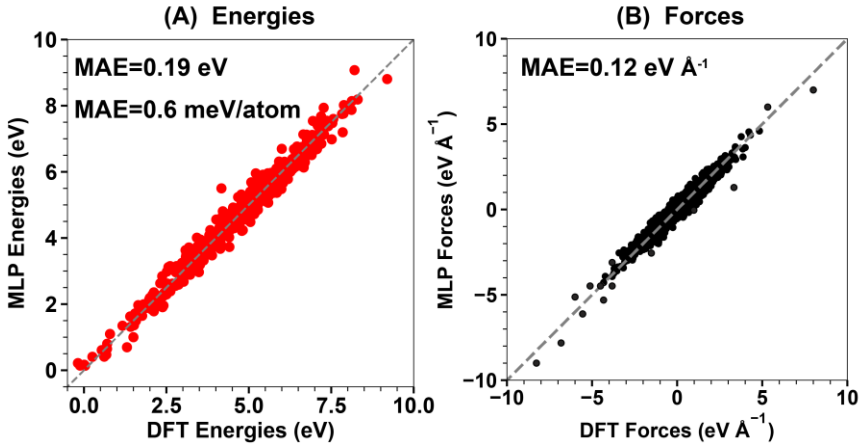

Supplementary Fig. 4. (A) Energies and (B) Forces predicted using the FLARE model during on-the-fly training (554 structures).

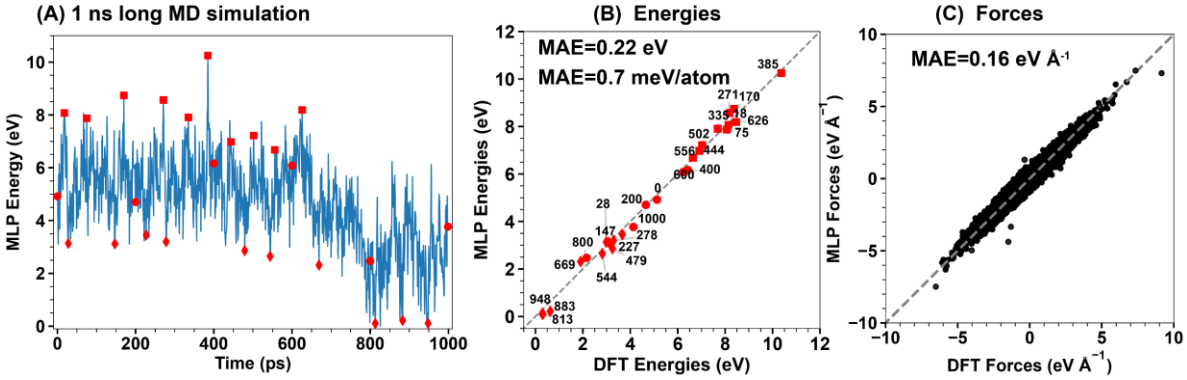

Supplementary Fig. 5. Validation of the FLARE MLP using DFT. Parity plots of (B) Energies and (C) Forces estimated from the FLARE potential vs DFT for $[Co(NH_3)_4]^{2+}$ in 4Al config. 4. MD simulation settings are T = 648 K (Nosé–Hoover thermostat), timestep = 0.5 fs and simulation time of 1 ns. For the model training, only the 4Al config.1 in MFI was used with other structures (clusters and CHA, Supplementary Scheme 1). Diamond, square, and circle symbols are local minima, local maxima, and structures that are 200 ps apart, respectively while simulation time (in ps) is shown in B for each structure obtained from the MD trajectory.

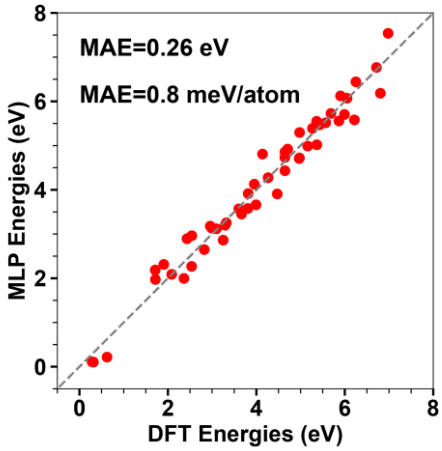

Supplementary Fig. 6. FLARE MLP and DFT energies of the 50 local minima structures identified for $[Co(NH_3)_4]^{2+}$ in five different 4Al configurations shown in Fig. 3A. The energies are relative to the lowest MLP energy structure (E=0).

Validation for $[Co(NH_3)_4\text{-}O_2\text{-}Co(NH_3)_4]^{4+}$/$[Co(NH_3)_4\text{-}O_2]^{2+}$ MLP

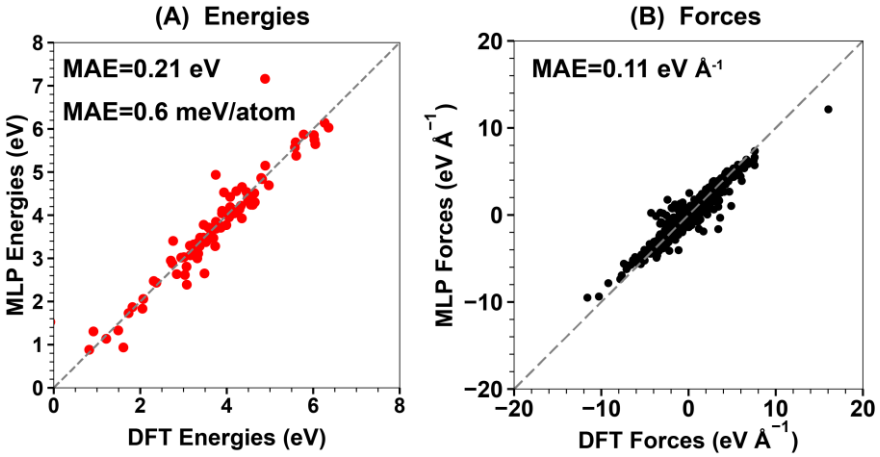

Supplementary Fig. 7. (A) Energies and (B) Forces predicted using the FLARE model during on-the-fly training (total 365 structures).

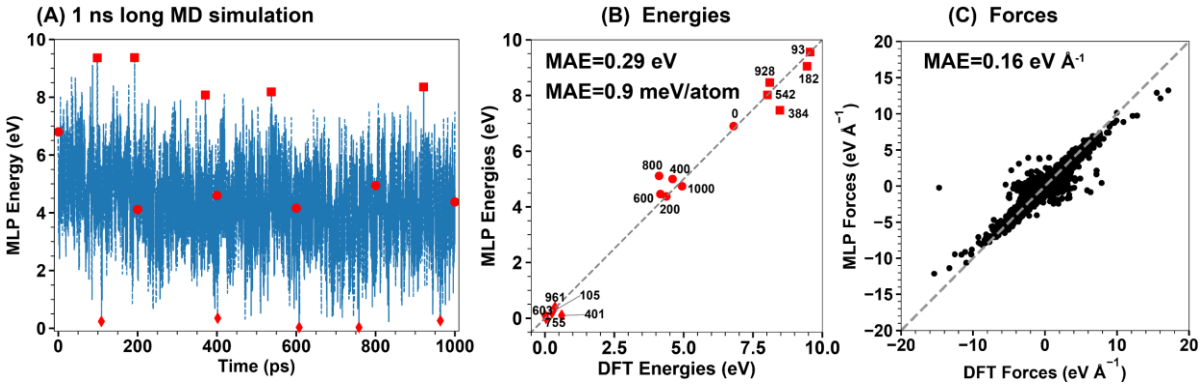

Supplementary Fig. 8. Validation of the FLARE MLP using DFT. Parity plots of (B) Energies and (C) Forces estimated from the FLARE potential vs DFT for $[Co(NH_3)_4]^{2+}$-O_2-$[Co(NH_3)_4]^{2+}$ in 4Al config. 4. MD simulation settings are T = 648 K (Nosé–Hoover thermostat), timestep = 0.2 fs and simulation time of 1 ns. For the model training, only the 4Al config.1 in MFI was used with other structures (clusters and CHA, Supplementary Scheme 1). Diamond, square, and circle symbols are local minima, local maxima, and structures that are 200 ps apart, respectively while simulation time (in ps) is shown in B for each structure obtained from the MD trajectory.

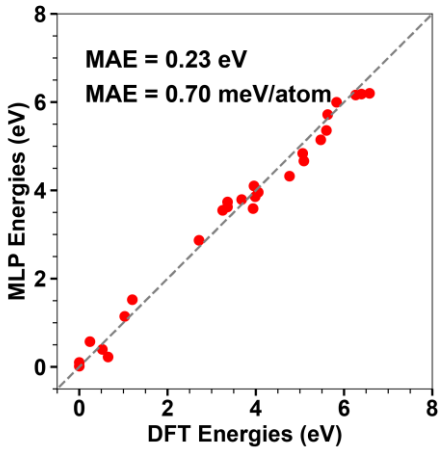

Supplementary Fig. 9. FLARE MLP and DFT energies of the 25 local minima structures identified for $[Co(NH_3)_4]^{2+}$-O_2-$[Co(NH_3)_4]^{2+}$ in five different 4Al configurations shown in Fig. 3A. The energies are relative to the lowest MLP energy structure (E=0).

MD simulations

Using the appropriate MLP for each system, we performed molecular dynamics using the Nosé–Hoover chain thermostat (*'NoseHooverChainNVT'*) implemented in ASE with a step size of 0.5 fs for 648 K simulations (except for 0.2 fs used for the dicobalt structure, which had stability issues when using higher timesteps) and 1 fs for 473 K simulations. We set the characteristic time scale for the thermostat (*tdamp*) to 100 timesteps and used three thermostat variables in the Nose-Hoover chain (*tchain* =3). The initial velocities of atoms were assigned from a Boltzmann distribution (as implemented in ASE) at simulation temperatures.

Structure sampling and entropy estimates from MD trajectories

Using the trained MLPs, we ran MD simulations for 1-6 ns for each species, and from each MD trajectory we sampled ten low energy candidate structures, that were sampled at least 1 ps apart, as initial guesses for DFT optimizations. Next, we performed spin-polarized, plane-wave, periodic DFT calculations (as described above).

We calculated the energies for single Co^{II} cations exchanged near 2Al configurations (main text Figs. 2E, F and Supplementary Figs. 34-35) that are either 2nd nearest neighbor (NN) or 3NN arrangements in the 5- and 6-membered rings of MFI. Prior work from Hibbitts and coworkers showed that Co^{II} ions preferentially exchange at these 2Al arrangements [3]. For simulations involving two Co^{II} cations we used five diverse 4Al configurations (main text, Fig. 3) that include superpositions of the 2Al configurations used for the single Co^{II} cation simulations. These 4Al configurations span a range of Al-Al distances (Fig. 3A, bottom five panels) and Co^{II} cation exchange energies (Supplementary Table 8).

All the reaction energies in the main text are calculated using DFT, with the aid of our MLPs to efficiently sample the minimum energy structures. For example, we sampled $[Co(NH_3)_x(H_2O)_y]^{2+}$ (x,y=0-6), and Co^{II} dimers, $[Co(NH_3)_zO_2Co(NH_3)_z]^{4+}$ (z=3-6) in MFI zeolite using our pretrained MLPs. Supplementary Fig. 10 shows all the local minima identified for 2 $[Co(NH_3)_4]^{2+}$ in the 4Al configuration 1 (minima for other 4Al configurations are given in SI files). Further, we used these long (> 1 ns) MD trajectories to estimate the entropy of solvated complexes using the quasi-harmonic approximation (QHA), details are in Supplementary Note5.

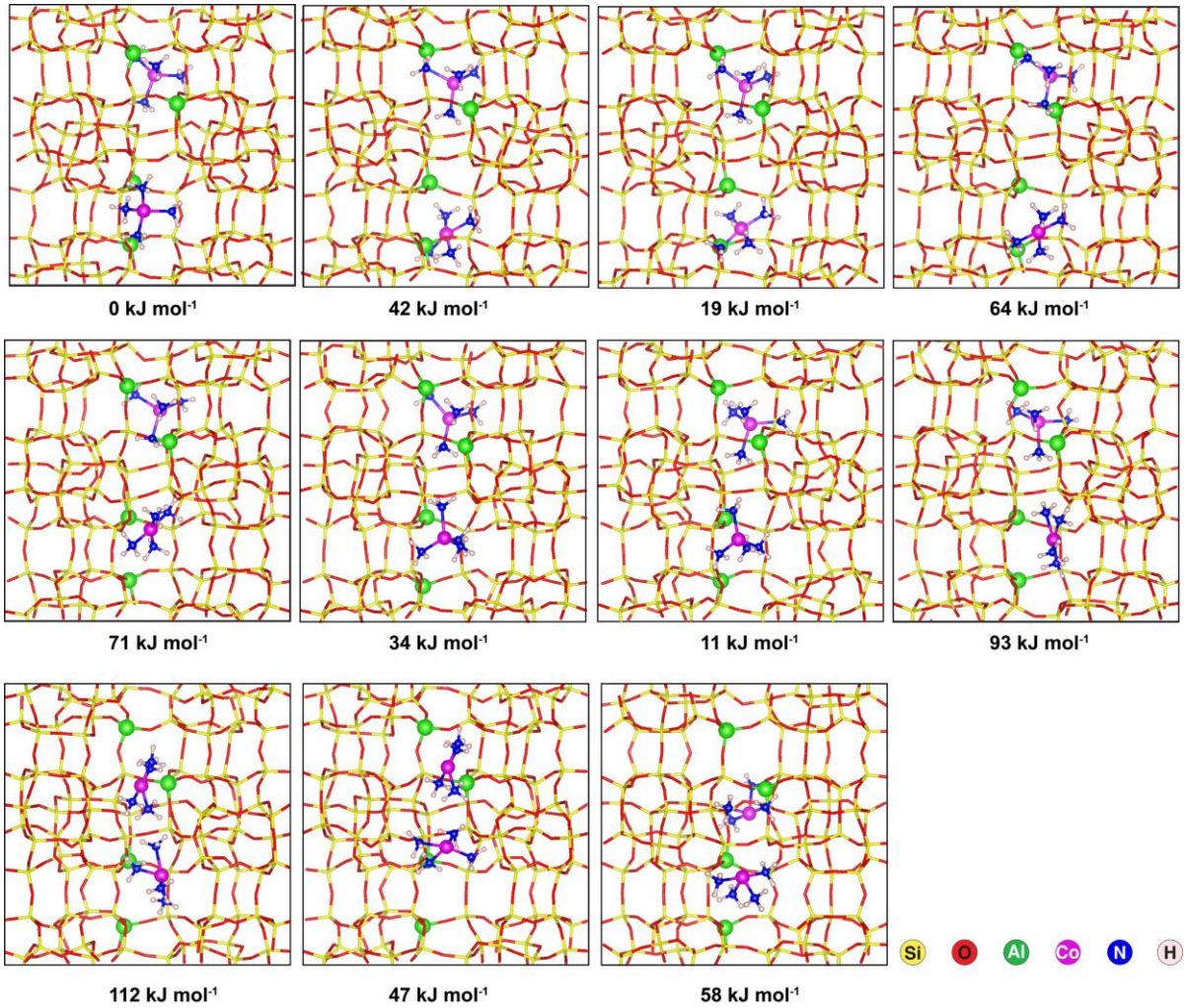

Supplementary Fig. 10. Minimum energy structures of 2 $[Co(NH_3)_4]^{2+}$ obtained from MD sampling. Relative energies of minima after DFT structure optimization are denoted below each structure.

Computed off-resonance Raman spectra

In prior work we computed frequencies and off-resonance Raman intensities in CHA zeolites [4], however, the large MFI cell makes similar computations here intractable due to computational cost. Moreover, because Co ions detach from the zeolite in the presence of NH_3, it is reasonable to neglect the zeolite and perform Raman intensity calculations on the isolated Co-ligand complexes. We computed off-resonance Raman spectra by first extracting DFT-optimized complexes ($[Co(NH_3)_4]^{2+}$, η^1-superoxo $[Co(NH_3)_4\text{-}O_2]^{2+}$, η^2-peroxo $[Co(NH_3)_4{=}O_2]^{2+}$, trans-μ-1,2-peroxo dicobalt $[Co(NH_3)_4\text{-}O_2\text{-}Co(NH_3)_4]^{4+}$) from MFI, followed by spin unrestricted DFT geometry optimizations in vacuum. We used Gaussian 16 and a universal background charge to set the net charge of the Co complex to +2 for monomers and +4 for dimers [5]. Functional sensitivity was evaluated using PBE [6], B3LYP [7], and M06 [8], all using the Def2TZVPP basis set. We used D3-BJ dispersion corrections for PBE and B3LYP calculations [9]. Becke-Johnson damping for M06 was unavailable in Gaussian 16, so we used D3 dispersion corrections instead [10]. Following geometry optimization, we computed Raman intensities using the same functional and basis set by differentiating dipole derivatives with respect to the electric field. Frequencies for each computed spectrum were subsequently scaled using the CCCBDB vibrational scaling factor database [11] according to the functional and basis set. M06 is not in the database, therefore we used the factor for M06-2X instead.

Supplementary Fig. 11 shows computed Raman spectra for the three functionals and four relevant Co complexes. The spectra correspond to the lowest energy spin state for each zeolite-encapsulated complex (Supplementary Table 4 reports all spin states used for Raman intensity calculations). Computed spectra were qualitatively consistent across all three functionals; PBE and B3LYP were quantitatively similar and M06 generally showed a shift in frequencies to higher wavenumbers. For main text Fig. 3D we used B3LYP due to its frequent use in literature for homogeneous Co complexes. Movies for the major vibrational modes discussed below are included as supplementary information attachment files.

For $[Co(NH_3)_4]^{2+}$, symmetric stretching ν(Co-NH_3) causes the large peak at ~350 cm^{-1} for PBE and B3LYP, and at ~400 cm^{-1} for M06. The ω(Co-NH_3) rocking vibrations are responsible for the shoulder near ~400 to 415 cm^{-1} for all three functionals.

For the η^1-superoxo species, $[Co(NH_3)_4\text{-}O_2]^{2+}$, the peak at ~250 cm^{-1} corresponds to ω(Co-NH_3) rocking without O_2 involvement. Across all functionals, the small peak located between 350-400 cm^{-1} corresponds to the ν(Co-NH_3) asymmetric stretch while the large peak near 400 cm^{-1} is from ν(Co-NH_3) symmetric stretching, both modes once again independent of the O_2 ligand.

The η^2-peroxo monocobalt, $[Co(NH_3)_4{=}O_2]^{2+}$, and trans-μ-1,2-peroxo dicobalt species, $[Co(NH_3)_4\text{-}O_2\text{-}Co(NH_3)_4]^{4+}$, were the only two structures that showed agreement with experimental spectra collected in flowing NH_3 and O_2 due to the presence of large intensity peaks between 400-500 cm^{-1}. For the peroxo, ν(Co-O_2) asymmetric stretching corresponds to peaks at 365 to 382 cm^{-1}, consistent with Co-O stretches reported for homogeneous complexes [12], while the complementary ν(Co-O_2) asymmetric stretch corresponds to peaks between 406 to 433 cm^{-1} for all functionals. Moreover, the peaks at 466, 468, and 493 cm^{-1} for PBE, B3LYP, and M06, respectively, are due to ω(Co-O_2) rocking. For $[Co(NH_3)_4\text{-}O_2\text{-}Co(NH_3)_4]^{4+}$ the small peaks around 397, 405, and 434 cm^{-1} for PBE, B3LYP, and M06, respectively, is a ν(Co-O_2-Co) asymmetric stretch. The largest peak at 415, 449, and 486 cm^{-1} for PBE, B3LYP, and M06,

respectively, correspond to ω(Co-O_2-Co) rocking involving the ammine ligands.

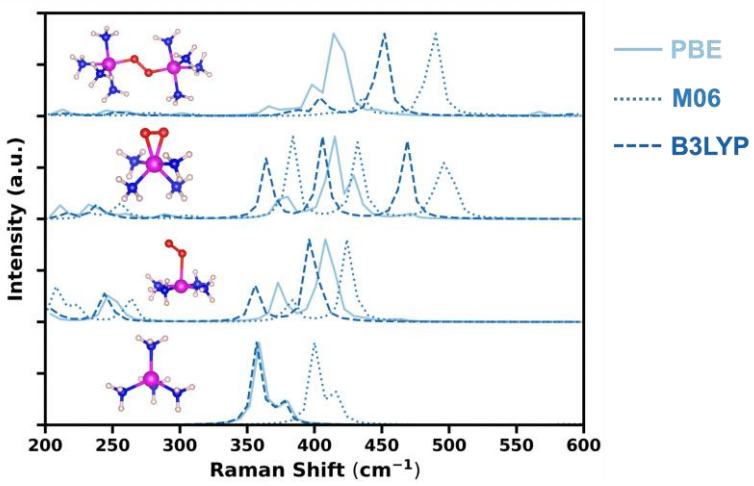

Supplementary Fig. 11. Computed off-resonance Raman spectra with different functionals for (top to bottom) *trans*-μ-1,2-peroxo dicobalt, η^2-peroxo-cobalt-tetraammine, η^1-superoxo-cobalt-tetraammine, and cobalt-tetrammine complexes.

Supplementary Table 4. Lowest energy spin states for each computed (Def2TZVPP basis set) species.

Cobalt Species	Spin State	Functional
$[Co(NH_3)_4]^{2+}$	quartet	B3LYP
$[Co(NH_3)_4]^{2+}$	quartet	PBE
$[Co(NH_3)_4]^{2+}$	quartet	M06
superoxo, $[Co(NH_3)_4\text{-}O_2]^{2+}$	doublet	B3LYP
superoxo, $[Co(NH_3)_4\text{-}O_2]^{2+}$	doublet	PBE
superoxo, $[Co(NH_3)_4\text{-}O_2]^{2+}$	doublet	M06
peroxo, $[Co(NH_3)_4{=}O_2]^{2+}$	doublet	B3LYP
peroxo, $[Co(NH_3)_4{=}O_2]^{2+}$	doublet	PBE
peroxo, $[Co(NH_3)_4{=}O_2]^{2+}$	doublet	M06
trans-μ-1,2-peroxo, $[Co(NH_3)_4\text{-}O_2\text{-}Co(NH_3)_4]^{4+}$	singlet	B3LYP
trans-μ-1,2-peroxo, $[Co(NH_3)_4\text{-}O_2\text{-}Co(NH_3)_4]^{4+}$	singlet	PBE
trans-μ-1,2-peroxo, $[Co(NH_3)_4\text{-}O_2\text{-}Co(NH_3)_4]^{4+}$	singlet	M06

Supplementary Note 1. Characterization Results of Co-ZSM-5 Catalysts

We prepared a series of Co-ZSM-5 catalysts with varying cobalt concentrations to control the proximity of cobalt ions within ZSM-5, anticipating that this would differently influence the reaction rates during the oxidative dehydrogenation and ammoxidation of ethane. It was significant to synthesize Co-ZSM-5 exclusively composed of Co^{II} ions stabilized at aluminum pair sites, without the presence of other cobalt species (e.g., Co_3O_4), to avoid their contribution to reaction rates. To achieve this, we conducted ion-exchange of NH_4-ZSM-5 with $Co(NO_3)_2 \cdot 6H_2O$ in an aqueous solution, varying the concentration of $Co(NO_3)_2 \cdot 6H_2O$ solution.

Supplementary Fig. 12 represents the cobalt concentrations of Co-ZSM-5 as a function of the concentration of $Co(NO_3)_2 \cdot 6H_2O$ solution used in the synthesis. The equilibrium process governs ion-exchange between zeolites and metal cations ($nHZ + M^{n+} \leftrightarrow MZ_n + nH^+$ or $n(NH_4)Z + M^{n+} \leftrightarrow MZ_n + nNH_4^+$) and follows the Langmuir adsorption. This behavior includes monolayer adsorption, uniform adsorption, no interaction between adsorbed species, and a finite number of adsorption sites. Consequently, the correlation between cobalt concentrations in the final catalysts and solution concentrations shows Langmuir adsorption behavior.

$$C_{Co^{II}} = \frac{C_{Co^{II},max} \cdot K_L \cdot C}{1 + K_L \cdot C} \qquad \textit{... Equation S1}$$

Where C_{CoII} represents the cobalt concentration of the catalyst ($mmol \cdot g_{cat}^{-1}$), C is the concentration of $Co(NO_3)_2 \cdot 6H_2O$ solution (mM), K_L is the isotherm constant, and $C_{CoII,max}$ is the maximum cobalt concentration of the catalyst. According to this equation, $C_{CoII,max}$ is 0.139 $mmol \cdot g_{cat}^{-1}$ and $K_L = 0.889$. Cobalt ions are exclusively stabilized at aluminum pair sites ($2\,HZ + Co^{II} \leftrightarrow Z_2Co + 2\,H^+$) [13, 14], so if all aluminum sites are paired, theoretical maximum cobalt concentration should be 0.481 $mmol_{Co} \cdot g_{cat}^{-1}$ (Co/Al = 0.5). However, the actual maximum cobalt concentration is significantly low at 0.139 $mmol_{Co} \cdot g_{cat}^{-1}$ (Co/Al = 0.14), indicating that only a quarter of the total aluminum sites in the ZSM-5, used in this study, are paired. The remaining three-quarters of the aluminum sites are either isolated aluminum or extraframework aluminum. Nonetheless, we successfully varied the cobalt concentrations from 0.025 $mmol_{Co} \cdot g_{cat}^{-1}$ to 0.139 $mmol_{Co} \cdot g_{cat}^{-1}$ in the catalysts.

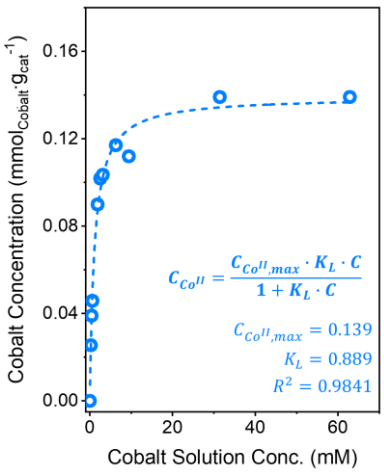

Supplementary Fig. 12. Cobalt concentration of Co-ZSM-5 as a function of concentration of cobalt solution used for ion-exchange.

Supplementary Fig. 13 displays the Ar physisorption for Co-ZSM-5 with the highest concentration (0.139 $mmol_{Co} \cdot g_{cat}^{-1}$) and H-ZSM-5. The minimal changes in the Ar isotherms before and after the cobalt incorporation indicate that the MFI framework remains intact after

the incorporation of Co^{II} ion. Supplementary Fig. 14 presents the X-ray diffractograms of these materials across the 2θ range of 5 to 50 °, including a detailed view from 35.5 to 38.5 °. The nearly identical diffractograms between them corroborate the Ar physisorption results. In addition, the absence of a peak at 2θ = 37 °, which corresponds to the primary diffraction pattern of Co_3O_4, confirms that substantially large Co_3O_4 particles do not exist in Co-ZSM-5.

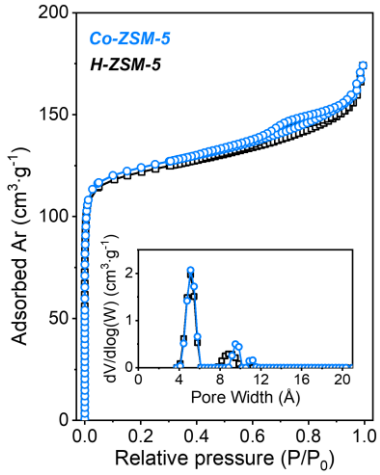

Supplementary Fig. 13. Ar physisorption on H-ZSM-5 and Co-ZSM-5. Inset figure displays their pore size distributions determined by non-local density functional theory (NL-DFT) models.

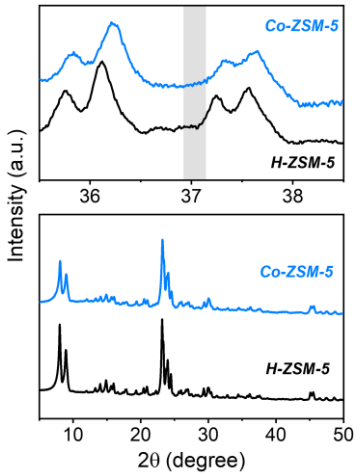

Supplementary Fig. 14. XRD patterns of H-ZSM-5 and Co-ZSM5 with magnified region.

We further characterized Co-ZSM-5 to confirm the exclusive presence of Co^{II} ions at aluminum pair sites using temperature programmed reduction, X-ray absorption spectroscopy, and UV-vis spectroscopy. Supplementary Fig. 15 demonstrates that no reduction peak appears up to 1100 K in Co-ZSM-5 with the highest concentration (0.139 $mmol_{Co} \cdot g_{cat}^{-1}$) in flowing H_2 (1 kPa), because the reduction of Co^{II} ions at aluminum pair sites hardly occurs below 1100 K [15, 16]. The white line of XANES spectrum of Co-ZSM-5 is distinct from those of Co foil and Co_3O_4 but closely resembles that of CoO (Supplementary Fig. 16A). Additionally, the edge position of Co-ZSM-5, determined as the maximum of the first-order derivatives, is 7721.2 eV nearly corresponding to that of CoO (7720.4 eV) rather than that of Co_3O_4 (7727 eV),

indicating that oxidation state of Co^{II} predominates (Supplementary Fig. 16B). More importantly, the EXAFS spectrum of Co-ZSM-5 shows only the first shell scattering from Co-O, with no additional scattering such as Co-{O}-Co arising from cobalt oxide or Co-Co arising from metallic cobalt (Supplementary Fig. 16C). These results suggest that most of cobalt species in Co-ZSM-5 are atomically dispersed Co^{II} ions interacting with anionic framework oxygen bonded to Al^{3+}, replacing Si^{4+}, without detectable amount of cobalt oxide or metallic cobalt.

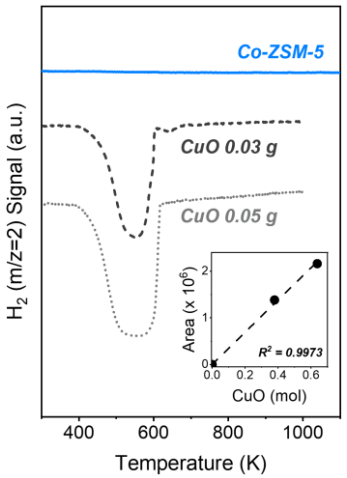

Supplementary Fig. 15. Temperature programmed reduction profiles by H_2 of Co-ZSM-5 and CuO reference. Inset figure represents calibration of H_2 consumption by area.

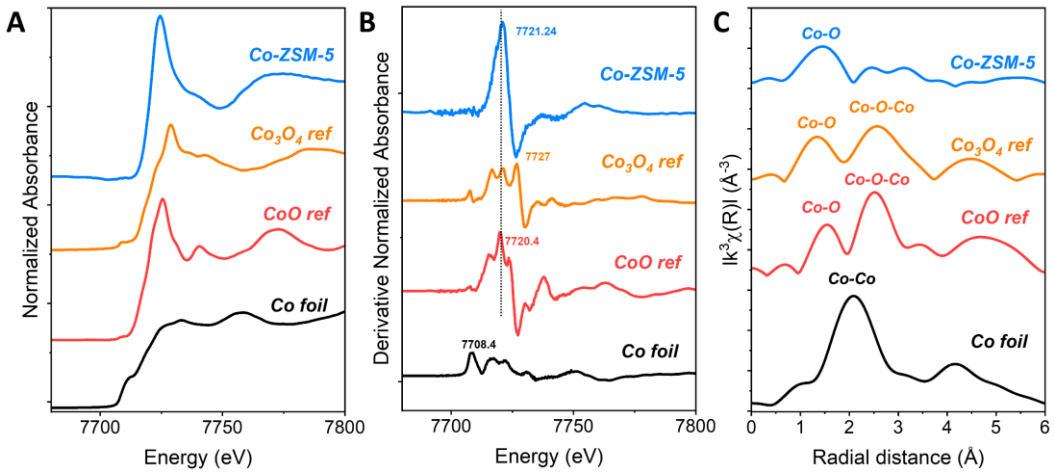

Supplementary Fig. 16. (A) Normalized XANES spectra, (B) first-order derivatives profiles, and (C) EXAFS spectra of Co-ZSM-5 with reference materials (Co foil, CoO, and Co_3O_4).

The exclusive presence of Co^{II} ions in Co-ZSM-5 with the highest cobalt concentration reasonably infers the sole presence of isolated Co^{II} ions at aluminum pair sites in the samples with lower cobalt concentrations. To provide experimental evidence on this, we analyzed the samples with lower cobalt concentrations using UV-vis spectroscopy under ambient conditions (Supplementary Fig. 17A). All samples exhibit a peak of cobalt d-d transition mainly at ~ 515 nm, which originates from d-d transition of Co^{II} ions octahedrally coordinated with H_2O, with no peaks indicative of cobalt oxide (345 nm, 380 nm, and 650 nm) [17]. For quantitative

analysis, the peak areas at ~515 nm of Co-ZSM-5 samples are correlated to their cobalt concentrations (Supplementary Fig. 17B). The quantification of cobalt species by the quantifiable Kubelka-Munk function demonstrates a linear correlation between the peak areas and cobalt concentrations ($R^2 = 0.9666$). Since Co-ZSM-5 with the highest cobalt concentration exclusively consists of the isolated Co^{II} ions stabilized at aluminum pair sites, the samples sticking to this linear line are also supposed to exclusively have Co^{II} ions. Consequently, Co^{II} ions stabilized at aluminum pair sites are the sole species present in all Co-ZSM-5 samples, regardless of cobalt concentrations. This uniformity allows us to rule out any potential contribution of heterogeneous cobalt species to turnover rates.

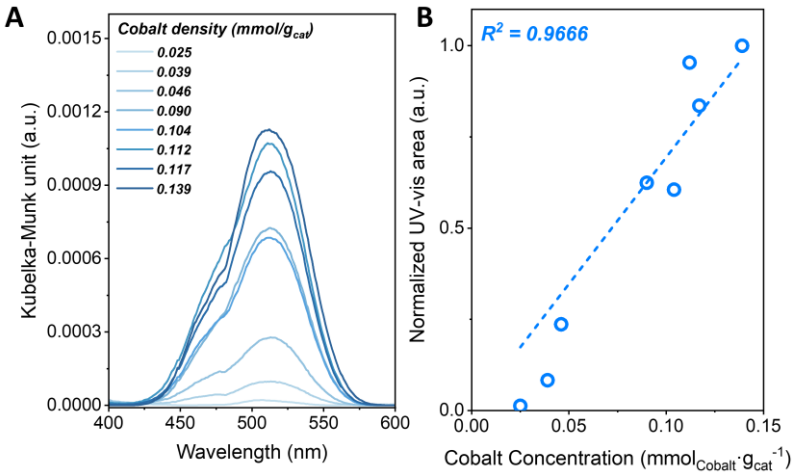

Supplementary Fig. 17. (A) UV-vis spectra of Co-ZSM-5 with varying cobalt concentrations and (B) correlation between cobalt concentrations and normalized areas within 450 – 550 nm arising from hydrated Co^{II} ions.

Supplementary Note 2. Rate Measurements

We investigated oxidative activation of ethane over Co-ZSM-5 under two different reaction conditions: oxidative dehydrogenation (O_2, C_2H_6) and ammoxidation (O_2, C_2H_6, NH_3). The oxidative dehydrogenation of C_2H_6 primarily produces C_2H_4, CO_2, and H_2O while ammoxidation forms CH_3CN, C_2H_6, and CO_2, as well as N_2, N_2O, H_2, and H_2O from the reactions involving NH_3. Supplementary Fig. 18 shows the selectivity of carbon-based products (CH_3CN, C_2H_4, CO_2) as a function of C_2H_6 conversion during oxidative dehydrogenation and ammoxidation reactions over Co-ZSM-5, measured by varying the contact time between the reactants and the catalyst. A short contact time (low conversion) between reactants and catalyst does not provide sufficient time for primary products to re-contact the active sites to transform into secondary products, resulting in the high selectivity of primary products. In contrast, a longer contact time (higher conversion) ensures enough time for primary products to undergo further reactions at the active sites to form secondary products, leading to a decrease in the selectivity of the primary products and an increase in the selectivity of secondary or tertiary products.

The oxidative dehydrogenation of C_2H_6 over Co-ZSM-5 primarily produces C_2H_4, with a small portion of CO_2, at the lowest conversion (Supplementary Fig. 18A). As the contact time (and thus the C_2H_6 conversion) increases, the selectivity for C_2H_4 decreases while the selectivity for CO_2 increases (Supplementary Fig. 18A). This indicates that C_2H_4 predominantly forms as a primary product of C_2H_6 conversion, whereas CO_2 majorly forms from the secondary oxidation of C_2H_4. Supplementary Fig. 18B shows that, during ammoxidation reactions, the selectivity for CH_3CN begins at a higher value but keeps decreasing with an increase in CO_2 selectivity while C_2H_4 selectivity does not significantly vary with appreciable value at the shortest contact time. This suggests that CH_3CN and C_2H_4 form primarily, and CO_2 forms by secondary reaction. The product selectivities are strongly dependent on the contact time between the reactants and the catalyst (conversion of C_2H_6), and it is challenging to precisely control the conversion of ethane over each Co-ZSM-5 sample. Nevertheless, since the reactant consumption is independent of secondary or tertiary reactions, focusing on the rate of C_2H_6 consumption allows for a more accurate comparison of the intrinsic activities of the active sites.

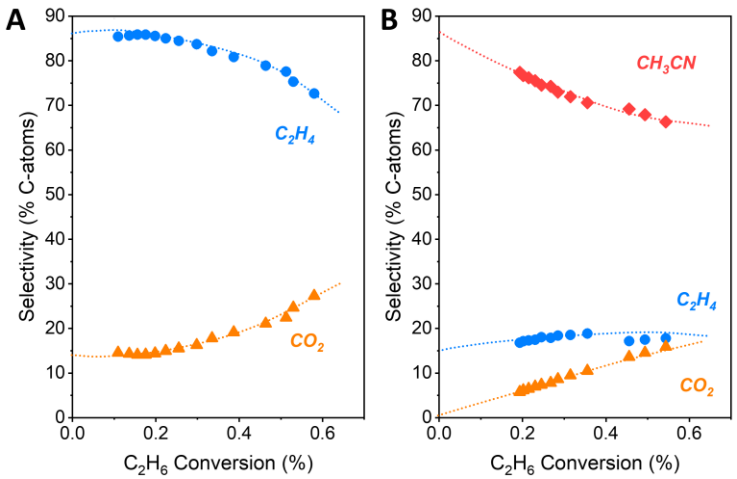

Supplementary Fig. 18. Carbon selectivities toward C_2H_4 ($S_{C,\,C2H4}$, ●), CO_2 ($S_{C,\,CO2}$, ▲), and CH_3CN ($S_{C,\,CH3CN}$, ◆) as functions of C_2H_6 conversion during reactions under (A) oxidative

dehydrogenation (7.5 kPa O_2, 5 kPa C_2H_6) and (B) ammoxidation (7.5 kPa O_2, 5 kPa C_2H_6, 5 kPa NH_3) conditions.

We performed rate measurements in the temperature range of 621 K to 661 K under oxidative dehydrogenation (7.5 kPa O_2, 5 kPa C_2H_6, Supplementary Fig. 19) and ammoxidation (7.5 kPa O_2, 5 kPa C_2H_6, 5 kPa NH_3, Supplementary Fig. 20) conditions. Control experiments revealed that H-ZSM-5 (calcined 773 K after two cycles of ammonium ion exchange, Methods in the main text) exhibits non-negligible catalytic activity (Supplementary Figs. 19A and 20A), which could stem from either intrinsic Brønsted acid sites or trace metal impurities (~ 0.01 $mmol_{Ni} \cdot g_{cat}^{-1}$ of Ni and ~ 0.004 $mmol_{Fe} \cdot g_{cat}^{-1}$ of Fe, confirmed by ICP-OES). Such impurities appeared despite the rigorous pretreatment with multiple ammonium ion-exchange and subsequent calcination, reflecting the inherent limitations in eliminating trace species sequestered within the zeolite.

To elucidate the nature of the background activity of H-ZSM-5 and rule it out from that of Co-ZSM-5, we first compared the mass-averaged reaction rates of H-ZSM-5 with different Si/Al ratios (11.5 and 15). Although H-ZSM-5 (Si/Al = 11.5) possesses a higher density of Brønsted acid sites, it exhibited a threefold lower C_2H_6 consumption rate compared to H-ZSM-5 (Si/Al = 15) (Supplementary Fig. 21A). This result indicates that the background activity does not primarily originate from Brønsted acid sites. Prior work by Li and Armor demonstrated that multiple metals, including Ni and Fe, catalyze ethane ammoxidation and produce similar products (CH_3CN, C_2H_4, CO_2) [18]. Our experiment using Ni-ZSM-5 (~ 0.03 $mmol_{Ni} \cdot g_{cat}^{-1}$) consistently demonstrates that nickel can convert C_2H_6 into these products (Supplementary Fig. 21B). Importantly, both H-ZSM-5 and Ni-ZSM-5 exhibit similar activation barriers ($E_{A,AMMOX}$ = 154 $kJ \cdot mol^{-1}$ and 150 $kJ \cdot mol^{-1}$, respectively) while Co-ZSM-5 displays a significantly lower barrier ($E_{A,AMMOX}$ = 122 ± 4 $kJ \cdot mol^{-1}$, Fig. 1B), suggesting that trace impurities (likely nickel) induce the background activity.

These distinct kinetic observations, alongside the order-of-magnitude higher rate on Co-ZSM-5 (0.139 $mmol_{Co} \cdot g_{cat}^{-1}$) compared to H-ZSM-5, indicate that cobalt-catalyzed and support-mediated pathways proceed independently. **Accordingly, we may isolate the ethane conversion chemistry at cobalt sites by subtracting the background activity of H-ZSM-5 from the catalytic activity of Co-ZSM-5.** This approach ensures that the reported kinetic and mechanistic insights reflect the dominant and intrinsic chemistry of the cobalt species, rather than the influence of support-induced factors.

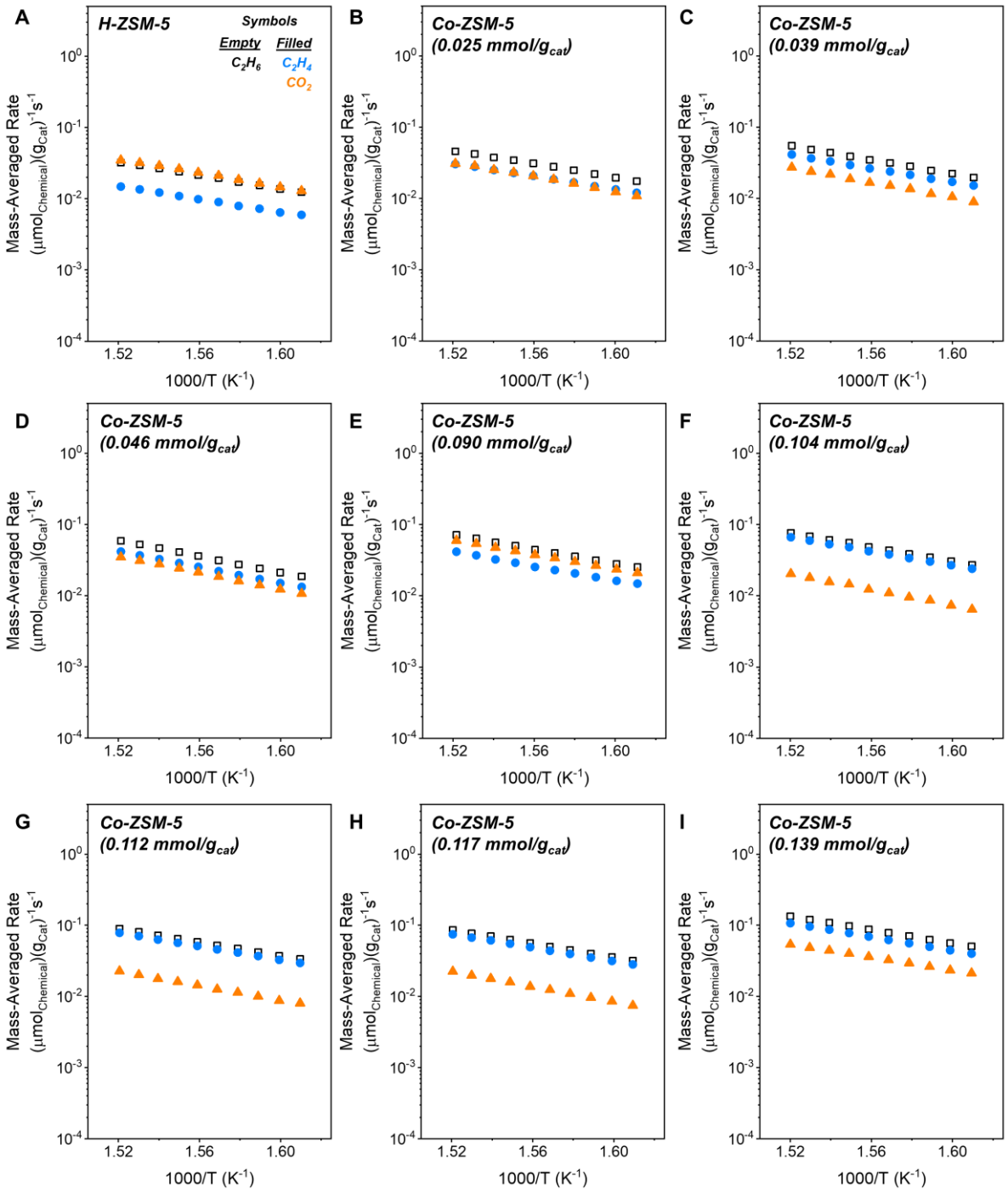

Supplementary Fig. 19. Temperature-dependent mass-averaged rates of C_2H_6 consumption (□), and product formation (C_2H_4 (●) and CO_2 (▲)) under oxidative dehydrogenation conditions (7.5 kPa O_2, 5 kPa C_2H_6) over (A) H-ZSM-5 and (B-I) Co-ZSM-5 with cobalt concentrations of (B) 0.025, (C) 0.039, (D) 0.046, (E) 0.090, (F) 0.104, (G) 0.112, (H) 0.117, and (I) 0.139 mmol·g_{cat}^{-1}.

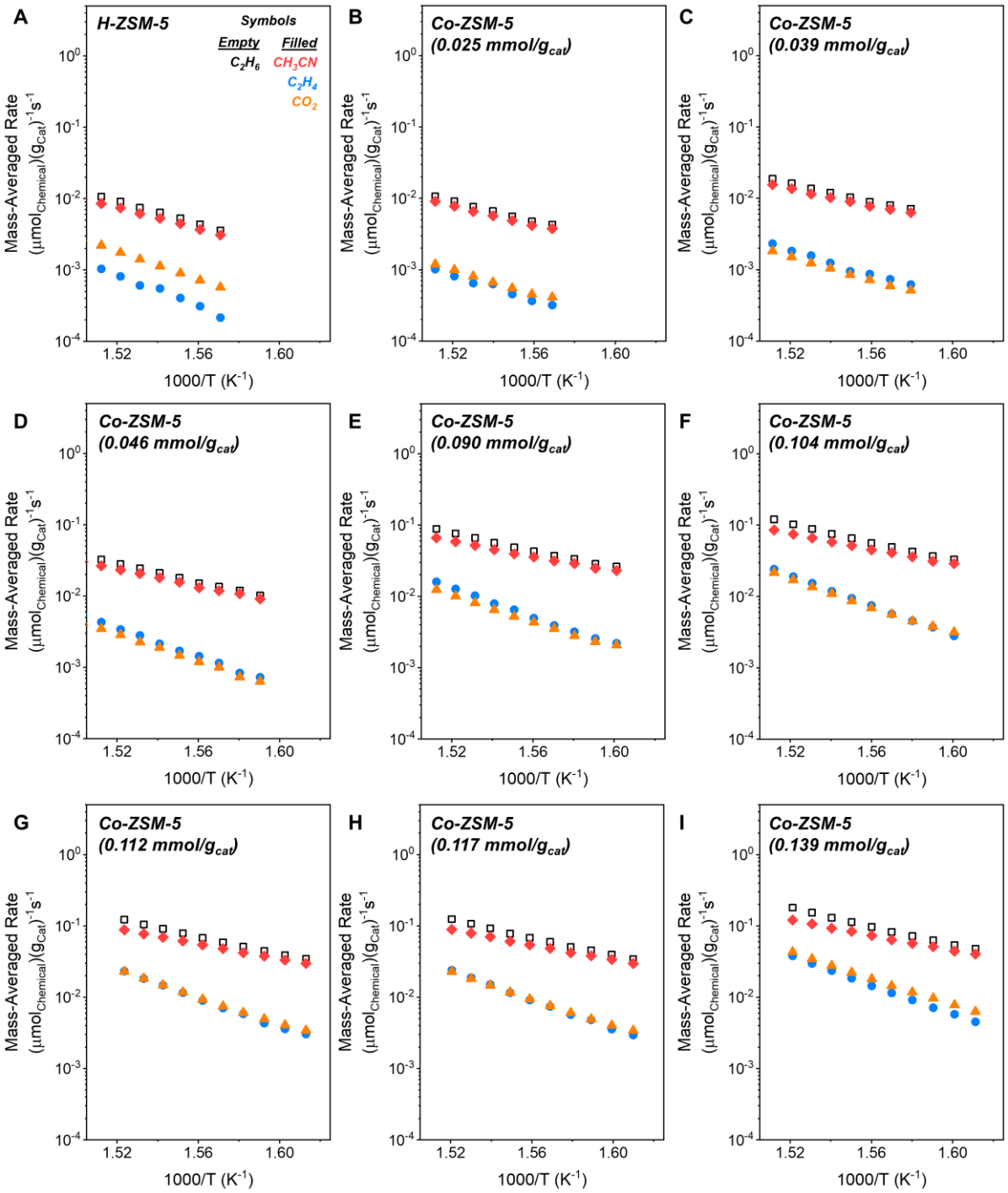

Supplementary Fig. 20. Temperature-dependent mass-averaged rates of C_2H_6 consumption (□), and product formation (CH_3CN (◆), C_2H_4 (●), CO_2 (▲)) under ammoxidation conditions (7.5 kPa O_2, 5 kPa C_2H_6, 5 kPa NH_3) over (A) H-ZSM-5 and (B-I) Co-ZSM-5 with cobalt concentrations of (B) 0.025, (C) 0.039, (D) 0.046, (E) 0.090, (F) 0.104, (G) 0.112, (H) 0.117, and (I) 0.139 mmol·g_{cat}^{-1}.

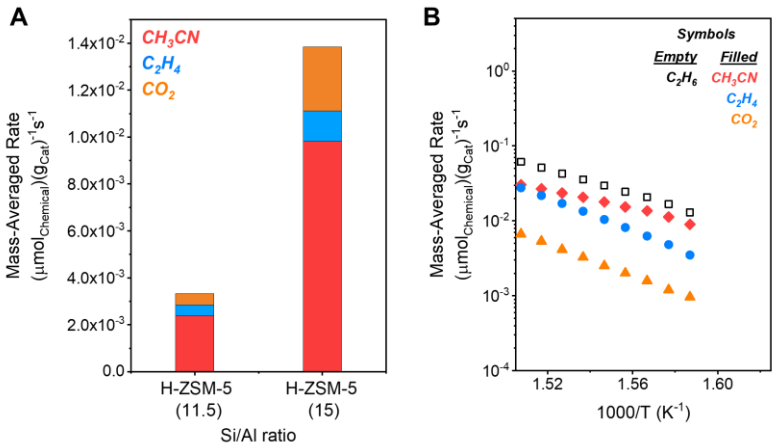

Supplementary Fig. 21. Mass-averaged rates of C_2H_6 consumption, and product formation (CH_3CN, C_2H_4, CO_2) under ammoxidation conditions (7.5 kPa O_2, 5 kPa C_2H_6, 5 kPa NH_3) over (A) H-ZSM-5 with different Si/Al ratios (11.5 vs. 15) at 665 K and (B) Temperature-dependent mass-averaged rates over Ni-ZSM-5 (0.03 $mmol_{Ni} \cdot g_{cat}^{-1}$).

Supplementary Note 3. *In situ* UV-vis spectra

Transition metals exhibit characteristic electron transitions between d-orbitals, with excitation energies typically falling within the ultraviolet and visible light ranges. Ligand-to-metal charge transfer (LMCT) or metal-to-ligand charge transfer (MLCT) alters these energy levels of d-orbitals, leading to distinct excitation energies of each metal-ligand complex [19]. Thus, UV-vis spectroscopy provides spectroscopic evidence for the presence of metal ions and metal-ligand complexes. We collected UV-vis spectra upon exposure to different gas compositions across a wide temperature range (303 – 673 K) (Supplementary Figs. 22-25, 27). However, temperatures may change the absorptivity of material, primarily due to alterations in either the local environment by thermal expansion of zeolites or thermal excitation of chemical species. In addition, Co-ZSM-5 undergoes coke formation under oxidative dehydrogenation (7.5 kPa O_2, 5 kPa C_2H_6) at reaction temperatures (> 573 K). This coke formation primarily occurs within the first few hours only under oxidative dehydrogenation conditions and becomes negligible after 24 hours of exposure at 621 K, as observed during rate measurements. However, the initial darkening of the sample significantly reduces the reflectance intensity, so all spectra were taken after 30 minutes of exposure, without 24 hours of stabilization period. Given these considerations, spectral comparisons focus on changes in the energy gap (peak position) driven by the metal-ligand interactions, rather than on changes in absolute absorbance, by using normalized spectra.

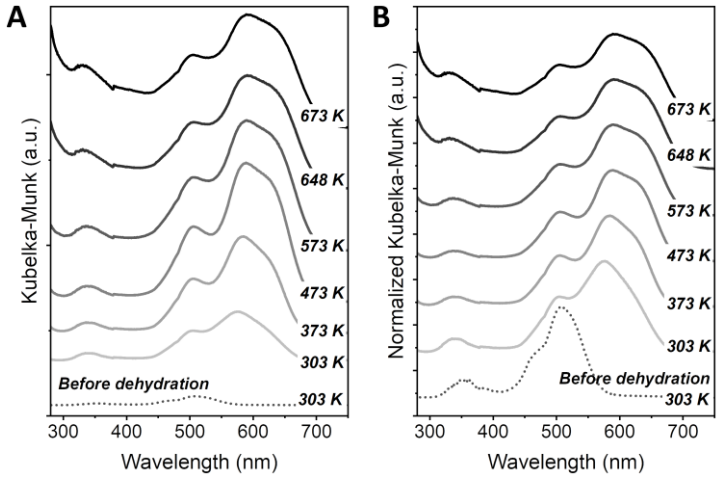

Supplementary Fig. 22. UV-vis spectra of Co-ZSM-5 in flowing Ar at 303 – 673 K (A) before and (B) after the normalization. Co-ZSM-5 was pretreated in flowing O_2 (10 kPa) at 573 K for 1 hour prior to the analysis.

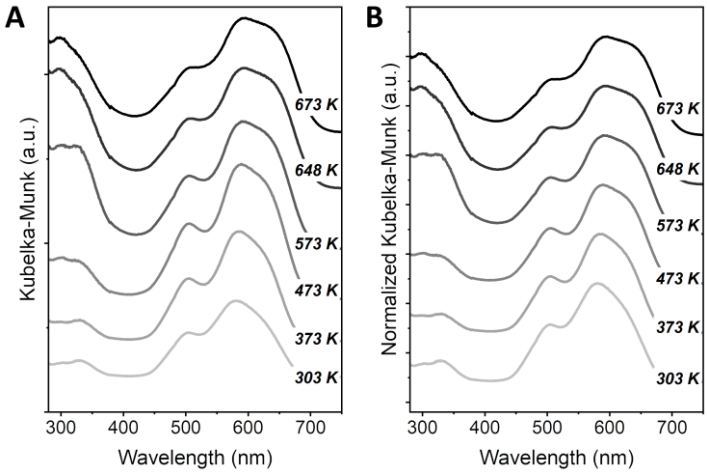

Supplementary Fig. 23. UV-vis spectra of Co-ZSM-5 in flowing O_2 (7.5 kPa) at 303 – 673 K (A) before and (B) after the normalization. Co-ZSM-5 was pretreated in flowing O_2 (10 kPa) at 573 K for 1 hour prior to the analysis.

The UV-vis features obtained in flowing oxygen (7.5 kPa O_2) match those collected in pure Ar across all temperatures tested but also possess an additional peak (335 nm) that corresponds to trivalent Co^{III} [20-23], likely corresponding to cobalt superoxo (Co^{III}-O_2^-). These spectra show that cobalt ions remain atomically dispersed and coordinated at 2Al sites as either Co^{II} or Co^{III}-O_2^- at these conditions.

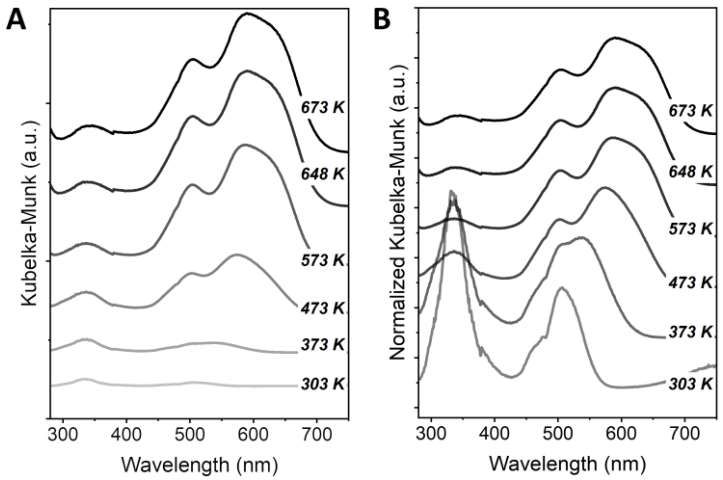

Supplementary Fig. 24. UV-vis spectra of Co-ZSM-5 in flowing H_2O (1 kPa) at 303 – 673 K (A) before and (B) after the normalization. Co-ZSM-5 was pretreated in flowing O_2 (10 kPa) at 573 K for 1 hour prior to the analysis.

The UV-vis spectra obtained in the presence of water vapor (1 kPa H_2O) indicate that water binds and may confer mobility to Co^{II} at low temperatures, as octahedral cobalt aquo complexes form at 303 – 373 K and cause the d-d transition at ~ 515 nm [19, 24]. However, the attenuation of this feature at higher temperatures shows the cobalt complexes dehydrate above 473 K and therefore remain as framework-bound Co^{II} ions at the reaction temperature (648 K). This

indicates that H_2O formed *in situ* cannot coordinate to Co^{II} strongly enough to impart mobility at the reaction temperatures of oxidative dehydrogenation of C_2H_6. At low temperatures, the peak at 335 nm may originate from the residual O_2 adsorbed during pretreatment, which desorbs with times or temperatures.

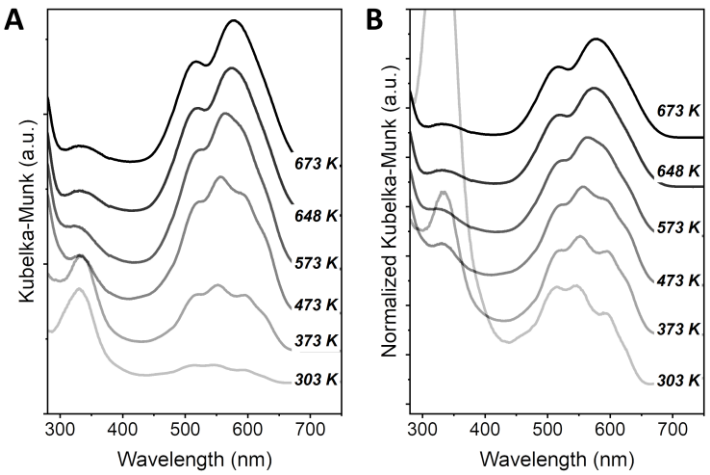

Supplementary Fig. 25. UV-vis spectra of Co-ZSM-5 in flowing NH_3 (5 kPa) at 303 – 673 K (A) before and (B) after the normalization. Co-ZSM-5 was pretreated in flowing O_2 (10 kPa) at 573 K for 1 hour prior to the analysis.

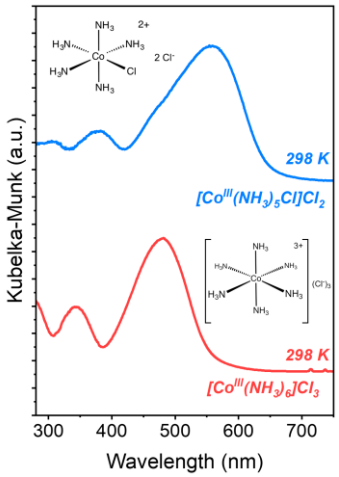

Supplementary Fig. 26. UV-vis spectra of $[Co^{III}(NH_3)_6]Cl_3$ and $[Co^{III}(NH_3)_5Cl]Cl_2$ at 298 K.

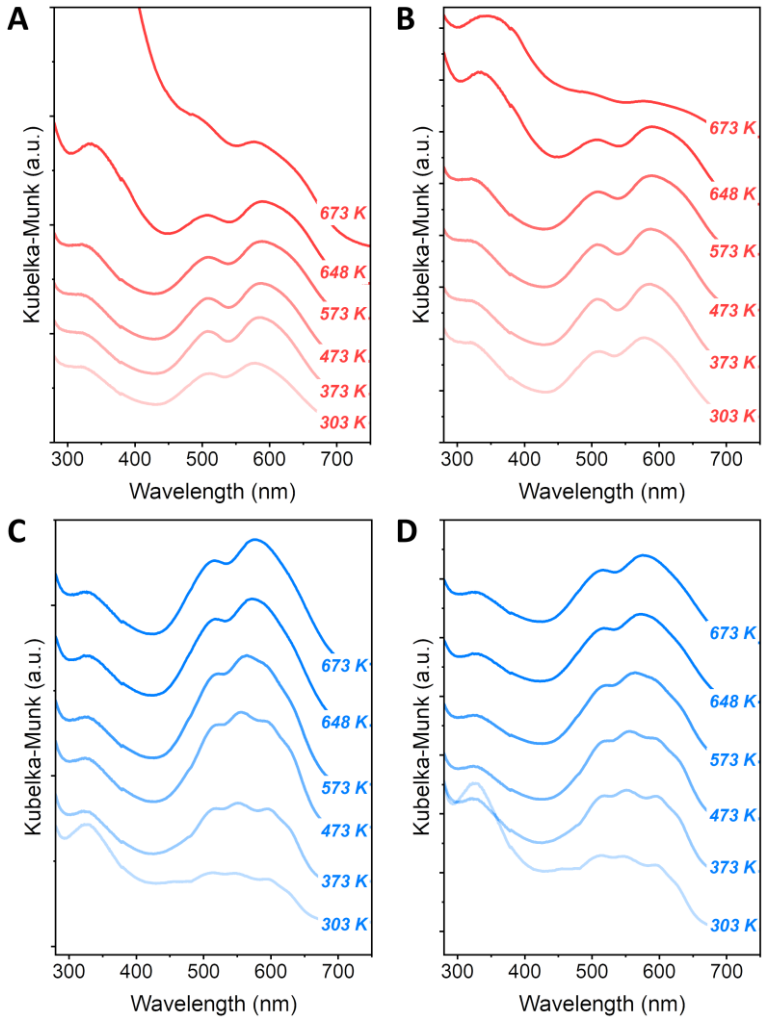

Supplementary Fig. 27. UV-vis spectra of Co-ZSM-5 at 303 – 673 K under (A, B) oxidative dehydrogenation (7.5 kPa O_2, 5 kPa C_2H_6) and (C, D) ammoxidation (7.5 kPa O_2, 5 kPa C_2H_6, 5 kPa NH_3) conditions. Figures show the spectra (A,C) before and (B, D) after the normalization. Co-ZSM-5 was pretreated in flowing O_2 (10 kPa) at 573 K for 1 hour prior to the analysis.

Supplementary Note 4. *In situ* XAS analysis

For the data analysis, CatXAS software [25] was used to correlate the LabVIEW and mass spectrometer data streams to the XAS spectra. CatXAS was also used to perform calibration and normalization on the transient XAS data. The spectra were energy calibrated by defining the maximum of the first derivative of the Co foil to be 7709.0 eV. The data recorded in steady state was further analyzed using Athena and Artemis packages of the Demeter software [26]. The Athena program was used to calibrate, align and merge the data. An average of 9 scans is used for the merging process to have a good signal to noise ratio. The EXAFS function, $\chi(k)$, was extracted by using a spline function and Fourier transformed in the 2.3-11.7 Å-1 k-range.

The results of k^2-weighted FT-EXAFS modeling performed in R-space using Co-{O}-Si/Al path (Supplementary Figs. 30-31) and Co-{O}-Co path (Supplementary Figs. 32-33) are summarized in Supplementary Tables 5-6. Note, the EXAFS modeling for the spectrum in flowing 5 kPa NH_3 at 298K has been performed using a limited R-space (1-2.2 Å) respect to all the other models (1-3.4 Å). The scattering paths used to model the EXAFS were generated using FEFF6 from the DFT optimized structures. The amplitude reduction factor value (S_0^2) was determined to be 0.81 by R-space modeling of the Co foil spectra (k^2-weighted, 3-12 Å-1 k-range, 1-5 Å R-range). The coordination numbers (CN), mean square deviation of interatomic distances (σ^2), energy shift (ΔE_0) and interatomic distances (R) parameters were refined for each fit during the modeling process.

The modeling using Co-{O}-Si/Al path fits well to the experimental data over the modeling using Co-{O}-Co path in all cases. The modeling of the O_2 + C_2H_6 spectrum using Co-{O}-Co path shows the negative coordination number for the second Co-O path, and its Red χ^2 is higher compared to the other model using Co-{O}-Si/Al path. In addition, its high σ^2 and ΔE_0 indicate the incorrect modeling using the wrong atom. Similarly, the modeling of other spectra (NH_3 and O_2 + C_2H_6 + NH_3) demonstrates the higher ΔE_0 and Red χ^2 when using Co-{O}-Co path. This indicates that dimeric species constitute only a portion, even during ammoxidation.

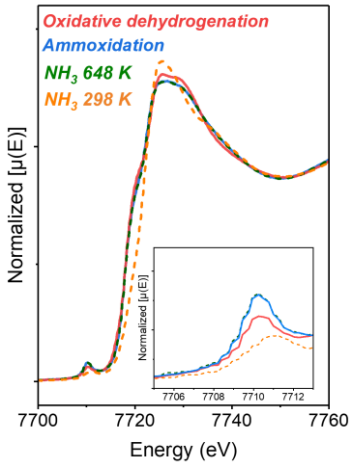

Supplementary Fig. 28. XANES spectra of Co-ZSM-5 obtained at reaction conditions for oxidative dehydrogenation (7.5 kPa O_2, 5 kPa C_2H_6) or ammoxidation (7.5 kPa O_2, 5 kPa C_2H_6, 5 kPa NH_3) at 648 K. The spectra in flowing 5 kPa NH_3 (Fig. 2B, main text) are displayed together for comparison.

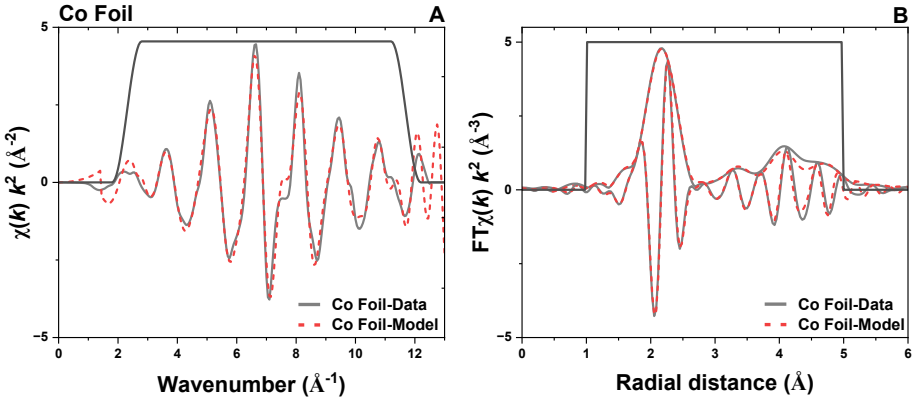

Supplementary Fig. 29. Data (grey) and relative model (red dotted) of (A) the k^2-weighted (3-12 Å^{-1} k-range, 1-5 Å R-range) spectra and (B) Fourier transformed EXAFS of the Co foil used to extract the S_0^2 value.

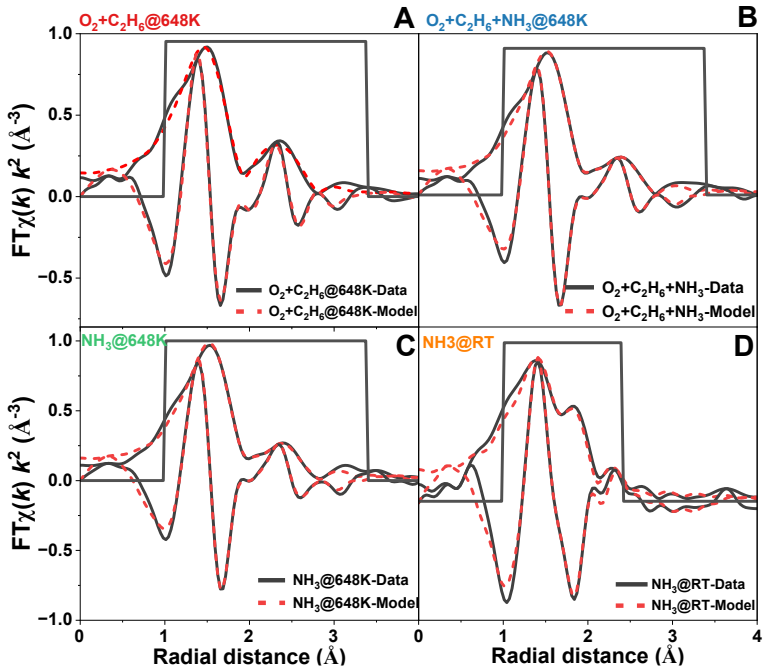

Supplementary Fig. 30. Data (grey) and relative model (red dotted) using Co-{O}-Si/Al path of imaginary part and magnitude of the k^2-weighted Fourier transformed EXAFS of Co-ZSM-5 in flowing (A) 7.5 kPa O_2 + 5 kPa C_2H_6 at 648 K, (B) 7.5 kPa O_2 + 5 kPa C_2H_6 + 5 kPa NH_3 at 648 K, (C) 5 kPa NH_3 at 648 K, and (D) 5 kPa NH_3 at ~ 308 K (R-range :1-3.4 Å, k-range:2.3-11.7 Å^{-1}). Note, the model for the spectrum obtained in flowing 5 kPa NH_3 at ~ 308 K has been performed using a reduced R-range (1-2.2 Å).

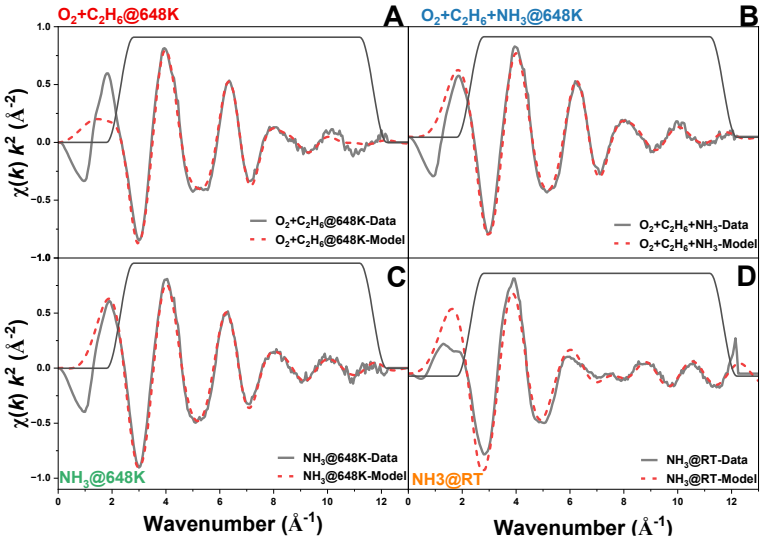

Supplementary Fig. 31. Data (grey) and relative model (red dotted) using Co-{O}-Si/Al path of k^2-weighted spectra (2.3-11.7 Å^{-1}) of Co-ZSM-5 in flowing (A) 7.5 kPa O_2 + 5 kPa C_2H_6 at 648 K, (B) 7.5 kPa O_2 + 5 kPa C_2H_6 + 5 kPa NH_3 at 648 K, (C) 5 kPa NH_3 at 648 K, and (D) 5 kPa NH_3 at ~ 308 K (R-range :1-3.4 Å, k-range:2.3-11.7 Å^{-1}).

Supplementary Table 5. Fit parameters obtained from EXAFS modeling of Co-ZSM-5 using Co-{O}-Si/Al path

Conditions		Scattering path	Radial distance (Å)	σ^2 (Å^2) × 10^3	Coordination number	ΔE_0 (eV)	R factor	Red χ^2
Gas	Temperature							
NH_3	298 K	Co-N/O	1.96 ±0.04	5.3 ±3.1	2.5 ±0.6	-0.9 ±2.1	0.01	2338
		Co-N/O	2.19 ±0.12		3.4 ±0.7			
	648K	Co-O/N	2.01 ±0.05	9.5 ±1.1	4.6 ±0.3	-0.3 ±0.7	0.005	145
		Co-{O}-Si/Al	2.77 ±0.1	6.2 ±8.7	0.7 ±0.6			
		Co-{O}-Si/Al	3.22 ±0.07		0.7 ±0.5			
O_2 + C_2H_6	648K	Co-O	1.96 ±0.04	12.4 ±3.3	4.8 ±1.1	-4 ±2.4	0.013	362
		Co-O	2.41 ±0.06		2.1 ±1.3			
		Co-{O}-Si/Al	3.11 ±0.07	14.6 ±5.6	4.5 ±1.8			
O_2 + C_2H_6 + NH_3	648K	Co-O/N	2.01 ±0.05	9.5 ±1.1	4.6 ±0.3	-0.5 ±0.8	0.006	315
		Co-{O}-Si/Al	2.77 ±0.02	8 ±12.7	0.8 ±1			
		Co-{O}-Si/Al	3.20 ±0.06		0.8 ±0.9			

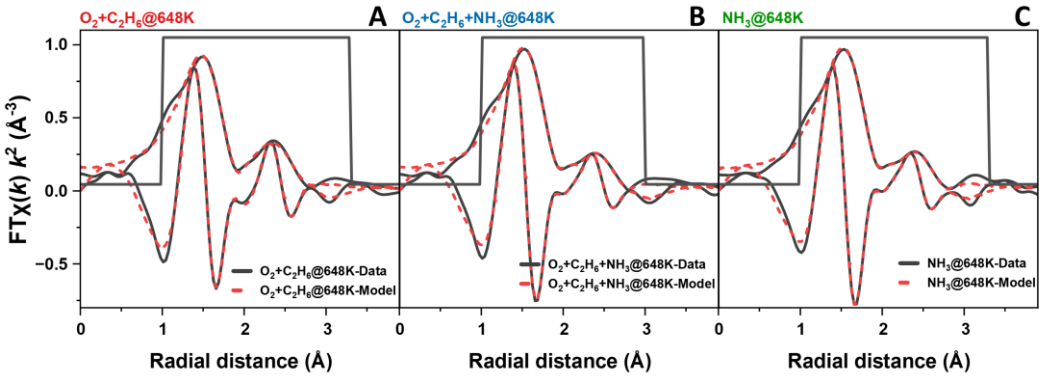

Supplementary Fig. 32. Data (grey) and relative model (red dotted) using Co-{O}-Co path of imaginary part and magnitude of the k^2-weighted Fourier transformed EXAFS of Co-ZSM-5 in flowing (A) 7.5 kPa O_2 + 5 kPa C_2H_6, (B) 7.5 kPa O_2 + 5 kPa C_2H_6 + 5 kPa NH_3, and (C) 5 kPa NH_3 at 648 K (R-range :1-3.4 Å, k-range:2.3-11.7 $Å^{-1}$).

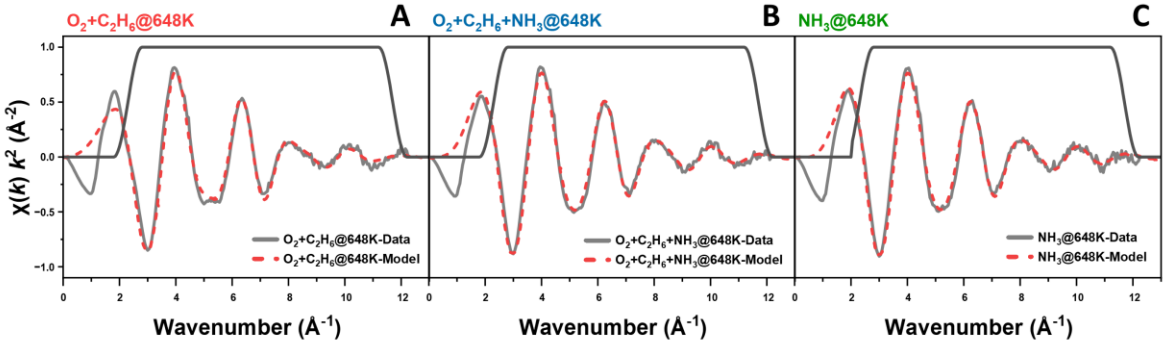

Supplementary Fig. 33. Data (grey) and relative model (red dotted) using Co-{O}-Co path of k^2-weighted spectra (2.3-11.7 $Å^{-1}$) of Co-ZSM-5 in flowing (A) 7.5 kPa O_2 + 5 kPa C_2H_6, (B) 7.5 kPa O_2 + 5 kPa C_2H_6 + 5 kPa NH_3, and (C) 5 kPa NH_3 at 648 K (R-range :1-3.4 Å, k-range:2.3-11.7 $Å^{-1}$).

Supplementary Table 6. Fit parameters obtained from EXAFS modeling of Co-ZSM-5 using Co-{O}-Co path

Conditions		Scattering path	Radial distance (Å)	σ^2 (Å^2) × 10^3	Coordination number	ΔE_0 (eV)	R factor	Red χ^2
Gas	**Temperature**							
NH_3	648K	Co-O/N	2.01 ±0.05	10 ±1	4.6 ±0.3	0.15±0.6	0.005	126
		Co-{O}-Co	2.9 ±0.11	17 ±6	2 ±1	-11 ±5		
O_2 + C_2H_6	648K	Co-O	1.97 ±0.05	10 ±4.3	4.3 ±1.1	-1.5±4.3	0.01	574
		Co-O	2.23 ±0.12		-0.95 ±1.8			
		Co-{O}-Co	2.89 ±0.12	19.7 ±7.3	4 ±2.3	-9.19±5		
O_2 + C_2H_6 + NH_3	648K	Co-O/N	2.00 ±0.05	9.6 ±1.1	4.6 ±0.3	-0.8±0.7	0.004	294
		Co-{O}-Co	2.91 ±0.10	16.7 ±6.1	1.9 ±1	-10.9±5		

Supplementary Note 5. Cobalt Speciation Predicted by Computation

Selecting different 2Al and 4Al configurations in MFI

The relative energies of Co^{II} species and interactions between framework and cations can vary significantly across different 2Al configurations and consequently, some 2Al configurations are more likely to exchange Co^{II} ions than others [3]. Our experimental Co-MFI samples have relatively low Co concentrations, and we expect the Co cations to be localized in the most energetically preferred ion exchange configurations. Therefore, for the calculations assessing the $\Delta G^{\text{form}}_{Z_2Co(NH_3)_x(H_2O)_y}$ (see below), we explored two different 2Al configurations in MFI with proximal Al ($d_{\text{min.Al-Al}} < 8$ Å) that energetically prefer Co^{II} exchange [3]. Similarly, for 4Al configurations we consider five configurations with four having proximal Al ($d_{\text{min.Al-Al}} < 8$ Å) in different combinations of 6 membered rings (MRs) and 5MRs and another 4Al configuration with isolated Al ($d_{\text{min.Al-Al}} >10$ Å) for comparison, although these 4Al configurations with isolated Al are less likely to exchange Co^{II} (see below).

Free Energy Calculations

We computed relative free energies of $[Co(H_2O)_{6-n}(NH_3)_n]^{2+}$, $[Co(H_2O)_n]^{2+}$ and $[Co(NH_3)_n]^{2+}$ (n = 0-6) species with respect to the Co^{II} (Z_2Co, where Z represents a framework Al) using the following reaction:

$$Z_2Co + x\ NH_3 + y\ H_2O \rightarrow Z_2Co(NH_3)_x(H_2O)_y \qquad \textit{... Equation S2}$$

The free energies of each species were evaluated using equations S3 and S4:

$$\Delta G^{\text{form}}_{Z_2Co(NH_3)_x(H_2O)_y}(T,\ \Delta\mu_{O_2},\ \Delta\mu_{H_2O}, \Delta\mu_{NH_3}) = \Delta E^{\text{form}}_{Z_2Co(NH_3)_x(H_2O)_y} - T\Delta S^{\text{QHA}}_{Z_2Co(NH_3)_x(H_2O)_y}(T) - x\,\Delta\mu_{NH_3} - y\,\Delta\mu_{H_2O} \qquad \textit{... Equation S3}$$

Here, $\Delta E^{\text{form}}_{Z_2Co(NH_3)_x(H_2O)_y}$ is the reaction energy of Equation S3 at 0 K, computed from DFT and $\Delta\mu_i$ ($\Delta\mu_i = \mu_i - \mu_i^\circ$) is the chemical potential of gaseous species between 0 K (μ_i°), and reaction conditions using the ideal gas law ($\mu_i(P,T)$) as per:

$$\mu_i(P,T) = \mu_i^\circ + RT\ln\left(\frac{P_i}{P^\circ}\right) \qquad \textit{... Equation S4}$$

where P° is the pressure at standard state = 1 atm. We used values listed in the NIST-JANAF database [27] for calculation of the chemical potential of the gas species (H_2O and NH_3).

Each solvated cationic complex can have numerous configurations with different energies and evaluating the free energy requires sufficient sampling of the potential energy surface. To accelerate the energy sampling of solvated complexes, we used a machine learning potential [28, 29] trained on DFT data per each structure (details of MLP training in Main test Methods) to perform molecular dynamics simulations. Next, from the molecular dynamics trajectories of 1 – 6 ns, we downsampled ten lower energy candidate structures per given stoichiometry and subsequently optimized with DFT to evaluate the energy, $\Delta E^{\text{form}}_{Z_2Co(NH_3)_x(H_2O)_y}$, in Equation S3.

For 4Al configurations in MFI, Equation S2 was replaced by

$Z_4Co_2 + x\ NH_3 + y\ H_2O + z\ O_2 \rightarrow [Z_2Co(NH_3)_x(H_2O)_y]\text{-}[O_2]_z$ / $[Z_2Co(NH_3)_x(H_2O)_y]$ or $[Z_2Co(NH_3)_x(H_2O)_y]\text{-}[O_2]_z\text{-}[Z_2Co(NH_3)_x(H_2O)_y]$ ***… Equation S5***

and Equation S3 was modified to include the Z_4Co_2 species and the chemical potential of O_2 (taken from the corresponding NIST-JANAF table). For the 4Al configurations, we followed the same structure sampling protocol using the appropriate MLP as for 2Al configurations.

Entropy estimates from MD trajectories

To calculate the translational, rotational and vibrational entropy components of adsorbed species, we used our MD trajectories (using the MLP) and the quasi-harmonic approximation (QHA).

$$S_{total}^{QHA} = S_{trans.}^{QHA} + S_{rot.}^{QHA} + S_{vib.}^{QHA} \quad \textit{… Equation S6}$$

Where,

$$S_{trans.}^{QHA} = R \ln\left[\left(\frac{24\pi\ e\ m\ k_B T}{h^2}\right)^{3/2} \sigma_1\sigma_2\sigma_3\right] \quad \textit{… Equation S7}$$

$$S_{rot.}^{QHA} = R \ln\left[\left(\frac{2\pi e k_B T}{h^2}\right)^{3/2} \left(\frac{8\pi^2\sqrt{I_1 I_2 I_3}}{\sigma_s}\right)\right] \quad \textit{… Equation S8}$$

$$S_{vib.}^{QHA} = R \sum_i^{3n-6} \frac{h\omega_i/k_B T}{exp(h\omega_i/k_B T)} - \ln[1 - exp(-h\omega_i/k_B T)] \quad \textit{… Equation S9}$$

In Equations S7-9, R is the universal gas constant, e is the Euler number, m is the mass of the adsorbate, k_B is the Boltzmann constant, and h is the Planck constant. σ_1, σ_2, and σ_3 are three principal root mean squared fluctuations of the center of mass of the ligand, calculated from the eigenvalues of the covariance matrix. In Equation S8, I_1, I_2, and I_3 are the average three principal moment of inertias calculated from the respective MD trajectory. The frequencies, ω_i , for $S_{vib.}^{QHA}$ are calculated from MD trajectories where for a structure with n atoms, the mass-weighted covariance matrix is obtained and then diagonalized to get 3n eigenvalues (λ_i). Then, 3n-6 non-zero (largest) quasi-harmonic frequencies are calculated from $\omega_i = \sqrt{k_B T\ /\ \lambda_i}$. Subsequently, we calculated S_{total}^{QHA} for all solvated (detached from the zeolite framework) Co complexes, and for zeolite framework bound Co species (e.g. Z_2Co), S is calculated from harmonic vibrational frequencies obtained from DFT (see below) and replaces the S_{total}^{QHA} term in Equation S3. Our calculations include zero-point energy (ZPE) effects because Equation S9 for vibrational free energy calculations includes ZPEs [30]. For phase diagrams and free energy diagrams at fixed conditions (Supplementary Figs. 32-35), we computed S_{total}^{QHA} at 473 K and 648 K using the MD trajectories at respective temperatures and

then extrapolated to other temperatures assuming a linear entropy variation vs temperature, as observed for other systems [2].

For comparison, we also estimated the entropy of extraframework species in the absence of the zeolite (referred to as gas phase species) using Gaussian's thermochemistry module at 1 atm pressure (Supplementary Table 7). Then, we calculated vibrational frequencies of extraframework species while keeping the framework atoms frozen to estimate the entropy using the harmonic approximation (HA). Frequencies below 100 cm^{-1} were neglected when computing entropies with HA. For all the phase diagrams and free energy calculations in this work, **we used entropies from QHA (detailed above, and in principle should be the most accurate method)** and experimental entropies from NIST database [27] for gaseous species such as O_2.

Supplementary Table 7. Entropy estimations from different methods. Entropy of species is estimated from QHA and harmonic approximation (HA) for $[Co(H_2O)_4]^{2+}$, $[Co(NH_3)_4]^{2+}$, and $[Co(NH_3)_4\text{-}O_2\text{-}Co(NH_3)_4]^{4+}$ at 473K and 648K. The average entropy across five different 4Al configurations is reported for QHA and HA methods and the column 'gas' reports the entropy of the complex in the absence of zeolite at 1 atm pressure.

	$[Co(H_2O)_4]^{2+}$ (J mol^{-1} K^{-1})			**$[Co(NH_3)_4]^{2+}$ (J mol^{-1} K^{-1})**			**$[Co(NH_3)_4\text{-}O_2\text{-}Co(NH_3)_4]^{4+}$ (J mol^{-1} K^{-1})**		
T	QHA	HA	gas	QHA	HA	gas	QHA	HA	gas
473 K	96	80	485	112	84	490	196	135	855
648 K	165*	120	548	186	142	560	241	147	1012

* Estimated from a shorter (16 ps) MD trajectory that excluded H_2O desorption events later in the simulation.

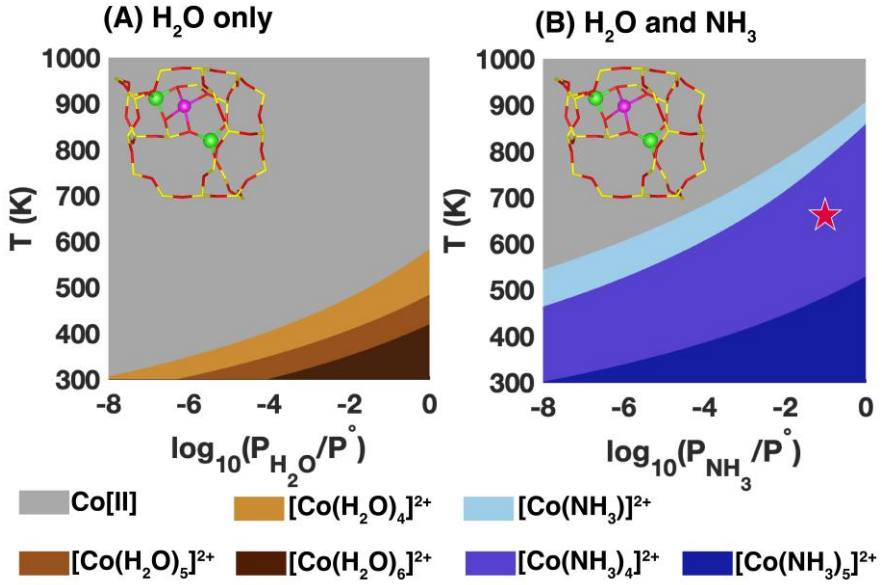

Supplementary Fig. 34. *Ab initio* phase diagrams for Co^{II} species in MFI for representative 2Al configuration in the 5-MR (4.9 Å separation), (A) with only water present and (B) both water and NH_3 present (0.5 kPa H_2O and 5 kPa NH_3). The star symbols signify the ammoxidation conditions (5 kPa NH_3).

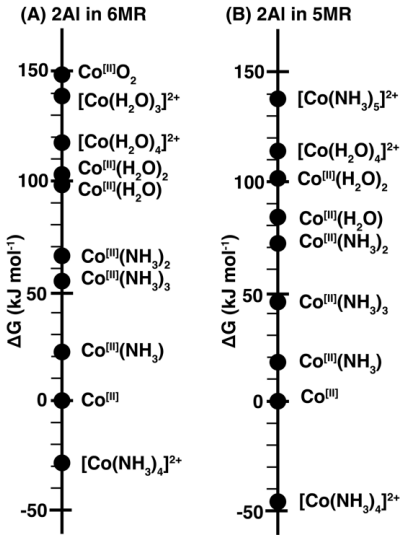

Supplementary Fig. 35. Free energies of species (no more than 150 kJ mol^{-1} less stable than zeolite bound Co^{II}) at a typical ammoxidation condition of 648 K and 5 kPa NH_3, 7.5 kPa O_2, 0.5 kPa H_2O for Co^{II} species located in different 2Al configurations.

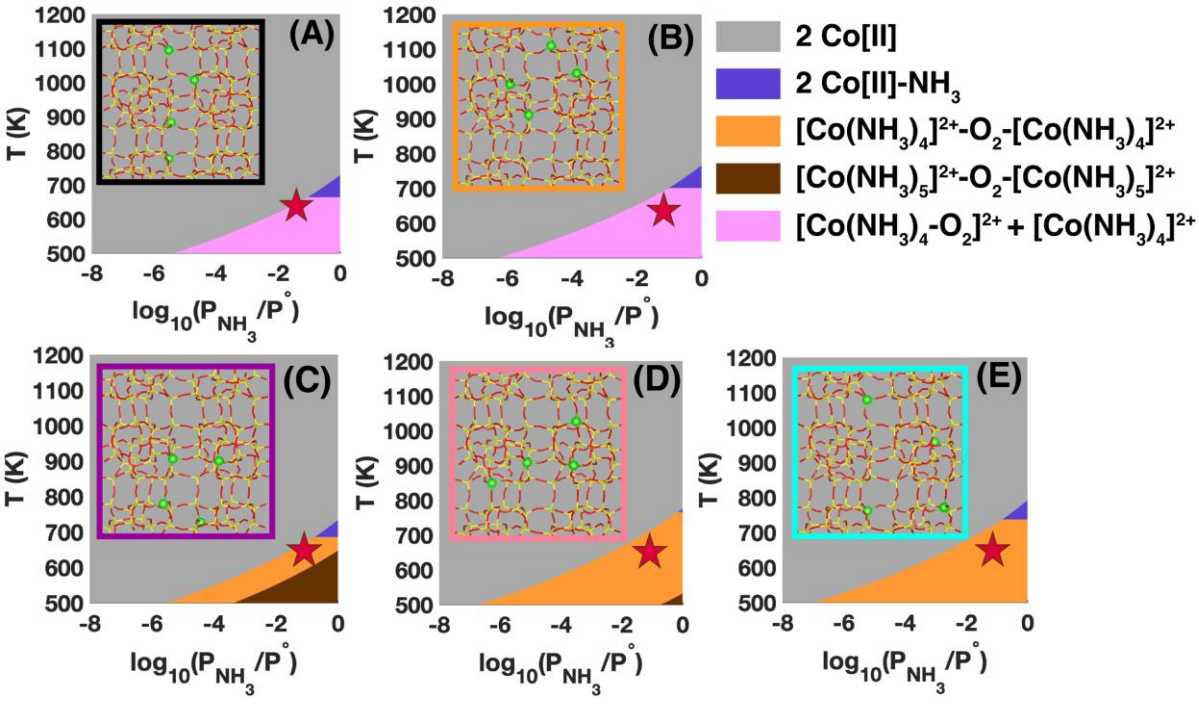

Supplementary Fig. 36. Thermodynamic phase diagrams for monomeric and dimeric sites at 7.5 kPa O_2, 0.5 kPa H_2O for Co^{II} species located in different 4Al configurations in MFI framework shown in the top left corner inset (atom colors: Al-green, Si-yellow and, O-red). The star symbol indicates a typical ammoxidation condition of 648 K and 5 kPa NH_3.

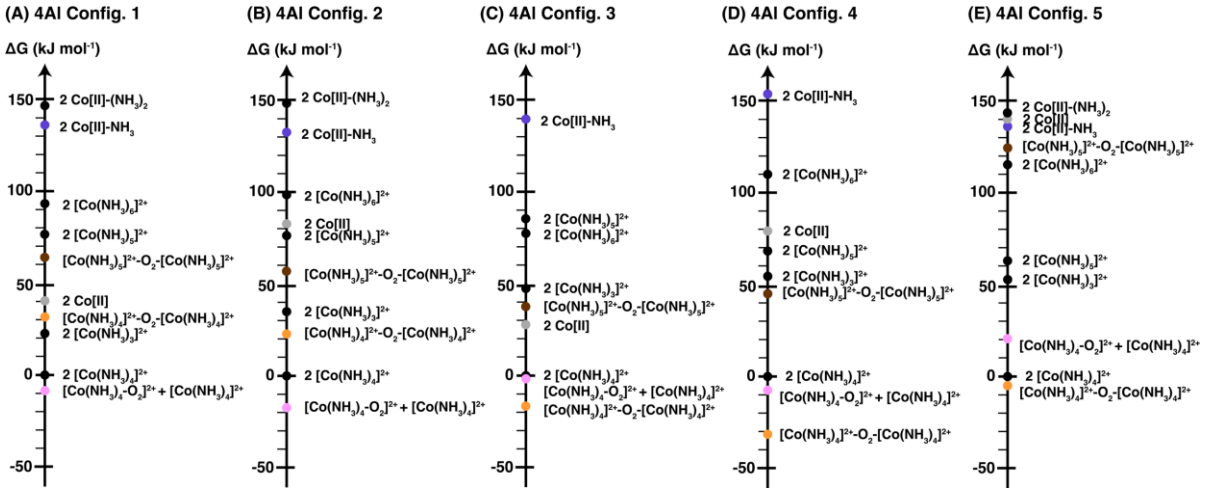

Supplementary Fig. 37. Free energies computed at a typical ammoxidation condition of 648 K and 5 kPa NH_3, 7.5 kPa O_2, 0.5 kPa H_2O for species (no more than 150 kJ mol^{-1} less stable than $[Co(NH_3)_4]^{2+}$) located in different 4Al configurations in MFI framework. The energy of $2[Co(NH_3)_4]^{2+}$ is set to 0 in each 4Al configuration, and species shown in Supplementary Fig. 36 have their respective colors.

Exchange energy estimates for the selected 4Al configurations in MFI

To determine the relative stability of NH_3-solvated Co exchanged at different Al configurations, for each of the 4Al configurations, we computed the Co exchange reaction energy (in the presence of NH_3) using:

$$Z_4(NH_4)_4\ (s) + 2CoO\ (s) + 4\ NH_3\ (g) \rightarrow 2[Z_2Co(NH_3)_4]\ (s) + 2\ H_2O\ (g) \quad \textbf{\ldots \textit{Equation S10}}$$

for each of the 4Al configurations shown in Fig. 3A, main text. The computed Cobalt exchange energies (0 K) are shown in Supplementary Table 8.

Supplementary Table 8: Cobalt exchange energies for each 4Al configuration in MFI computed using DFT (0 K, PBE-D3(BJ)).

4Al configuration	Co exchange energy kJ mol^{-1}	Relative Co exchange energy kJ mol^{-1}
config 1 (Al in 6MRs, para positions) black	-292	0
config 2 (Al in 5MRs, 2NN) orange	-225	67
config 3 (Al in 6MR and 5MR) purple	-256	36
config 4 (Al in 6MRs, meta and para positions) pink	-159	133
config 5 (isolated Al, any $d_{Al\text{-}Al}$ >10 Å) teal	-45	247

Structural analysis of extraframework species

Estimating the minimum distance between framework and extraframework atoms

We used ase built in *get_distances()* function with periodic boundary conditions enabled (*mic=True*) to compute the minimum distance between framework oxygen atoms and the Co center (Supplementary Fig. 38).

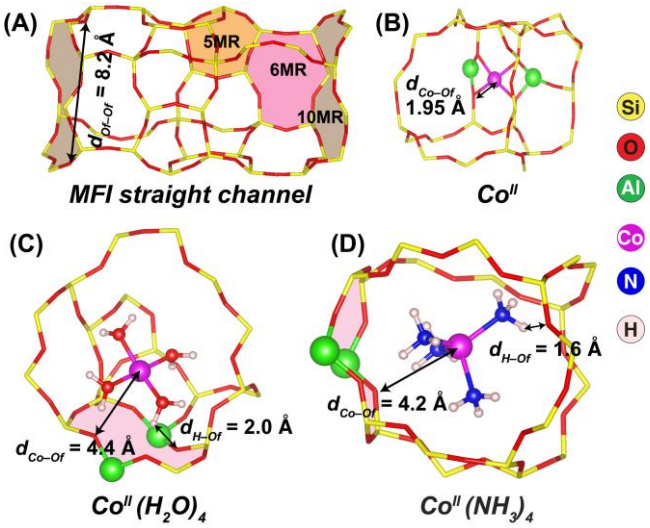

Supplementary Fig. 38. (A) MFI straight channel and the minimum distances, $d_{O—H}$ and $d_{Co—O}$ for species in Figs. 2D-F (main text): (B) Co^{II} , (C) $[Co(H_2O)_4]^{2+}$, and (D) $[Co(NH_3)_4]^{2+}$.

The tetrahedral index for $[Co(NH_3)_4]^{2+}$

To distinguish tetrahedral and square planar geometries of $[Co(NH_3)_4]^{2+}$ we calculated the structural index parameter τ4′ [31] defined by the two largest valence angles of coordination center (α and β) as follows.

$$\tau_4' = \frac{(\beta-\alpha)}{(360-\theta)} + \frac{(180-\beta)}{(180-\theta)} \quad \textit{... Equation S11}$$

The angles $\boldsymbol{\alpha}$ and $\boldsymbol{\beta}$ ($\boldsymbol{\beta} > \boldsymbol{\alpha}$) were computed using ase.get_angles() function, including the periodic boundary conditions and $\boldsymbol{\theta}$ is the tetrahedral angle ($\boldsymbol{\theta} = \mathbf{109.5°}$). Supplementary Fig. 39 shows the τ4′ structural index parameters over the 1 ns of simulation time for the two $[Co(NH_3)_4]^{2+}$ located in the five 4Al configurations.

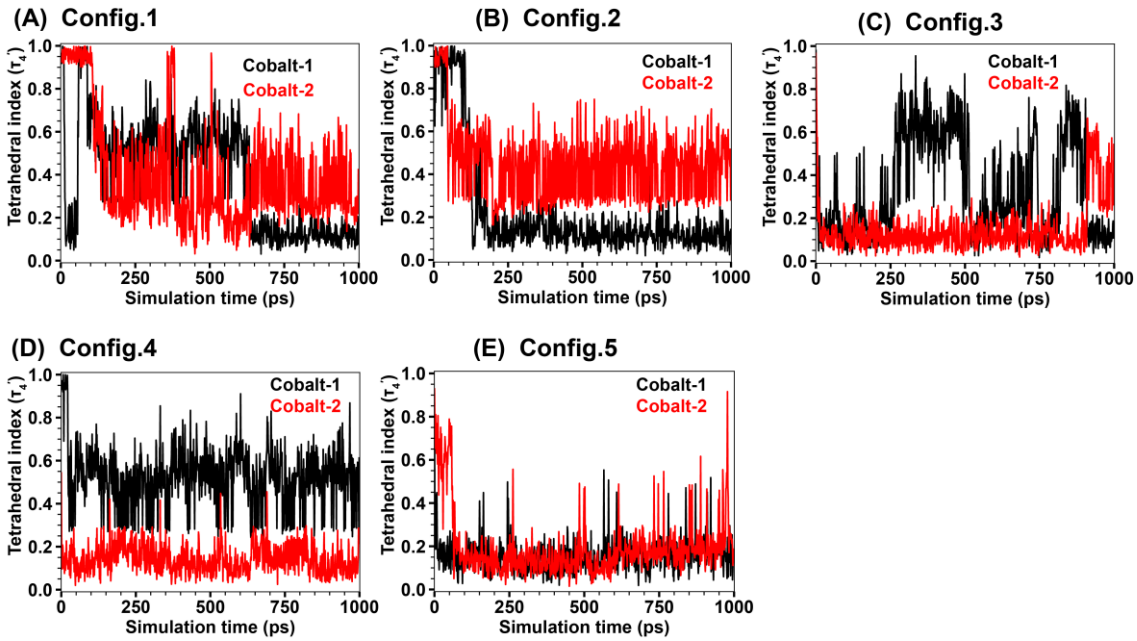

Supplementary Fig. 39. Variation of τ4′ structural index parameter over the 1 ns of simulation time for the two $[Co(NH_3)_4]^{2+}$ (Cobalt-1 and Cobalt-2) located in five 4Al configurations. A structure with τ4′ = 1.0 has a perfect tetrahedral coordination and τ4′ = 0 has a perfect square planar coordination.

Discrimination criteria for superoxo and peroxo geometries of $[Co(NH_3)_4\text{-}O_2]^{2+}$

We used cobalt-oxygen distances to distinguish superoxo- and peroxo-cobalt-ammine. For the two extra framework oxygen atoms ($\mathbf{O}_{e.f.}$), we computed distances $\boldsymbol{d_{Co-Oe.f.1}}$ and $\boldsymbol{d_{Co-Oe.f.2}}$ and the complex is categorized as peroxo if both distances are less than 2.5 Å, whereas only one of $\boldsymbol{d_{Co-Oe.f.}}$ < 2.5 Å and the other $\boldsymbol{d_{Co-Oe.f.}}$ > 2.5 Å defines the superoxo complex, and both $\boldsymbol{d_{Co-Oe.f.}}$ > 2.5 Å defines physisorbed O_2. We evaluated these distance criteria at 1 ps intervals of MD trajectories, for 1 ns for each of the five 4Al configurations in MFI (Supplementary Fig. 40).

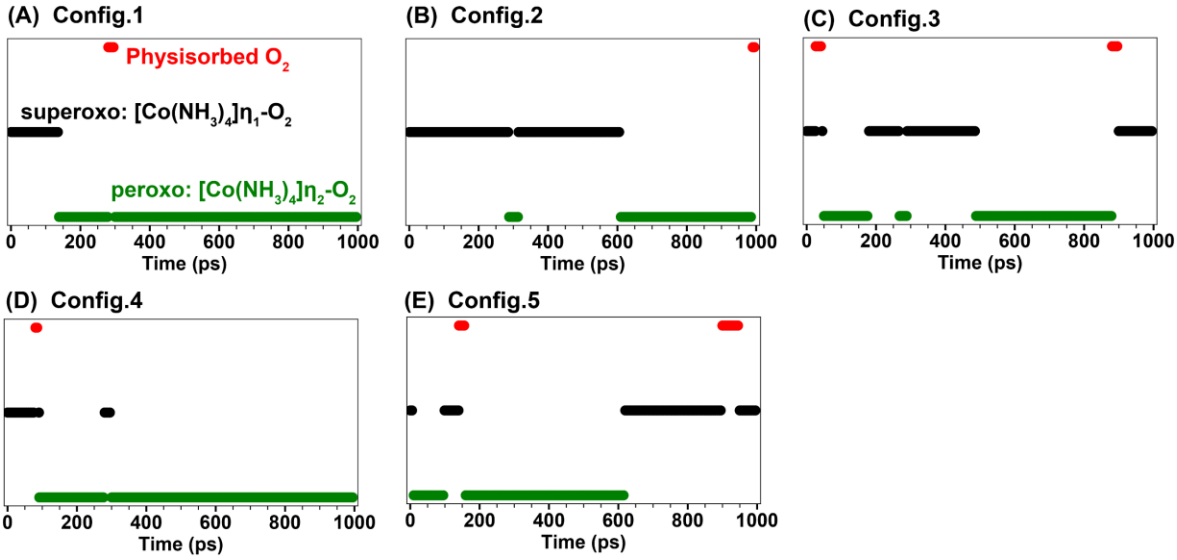

Supplementary Fig. 40. Time spent as peroxo, superoxo, and physisorbed O_2 species for each 4Al configuration.

Mobility of species located in 2Al configurations

We computed the center of mass of each NH_3 ligand bound to Co using ase *'get_center of mass()'* function and plotted the center of mass of each ligand sampled for the total simulation time of 1 ns. For visualization of the center of mass, we used a sphere with a 2.6 Å diameter, approximating the kinetic diameter of NH_3.

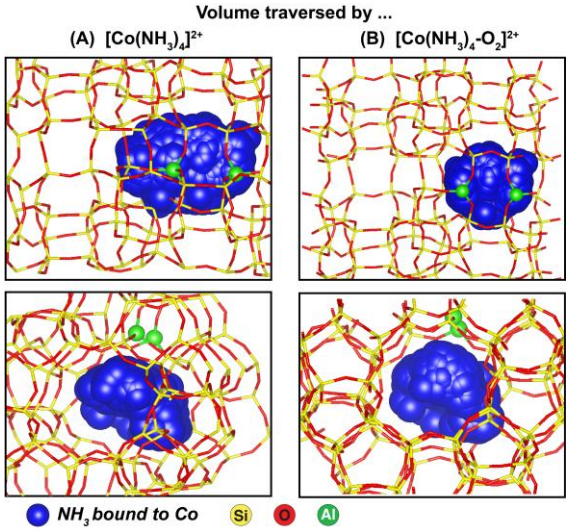

Supplementary Fig. 41. Mobility of each species during 1 ns MD simulations for the 2Al config.1 (2Al in 6MR). (A) $[Co(NH_3)_4]^{2+}$ and (B) $[Co(NH_3)_4\text{-}O_2]^{2+}$.

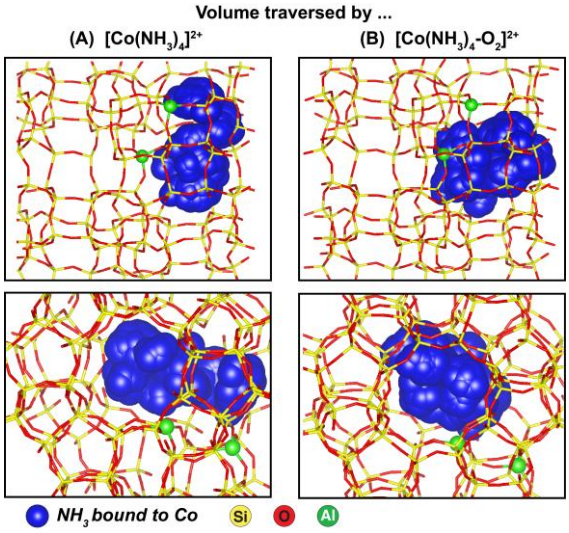

Supplementary Fig. 42. Mobility of each species during 1 ns MD simulations for the 2Al config.2 (2Al in 5MR). (A) $[Co(NH_3)_4]^{2+}$ and (B) $[Co(NH_3)_4\text{-}O_2]^{2+}$.

Mobility of species located in 4Al configurations

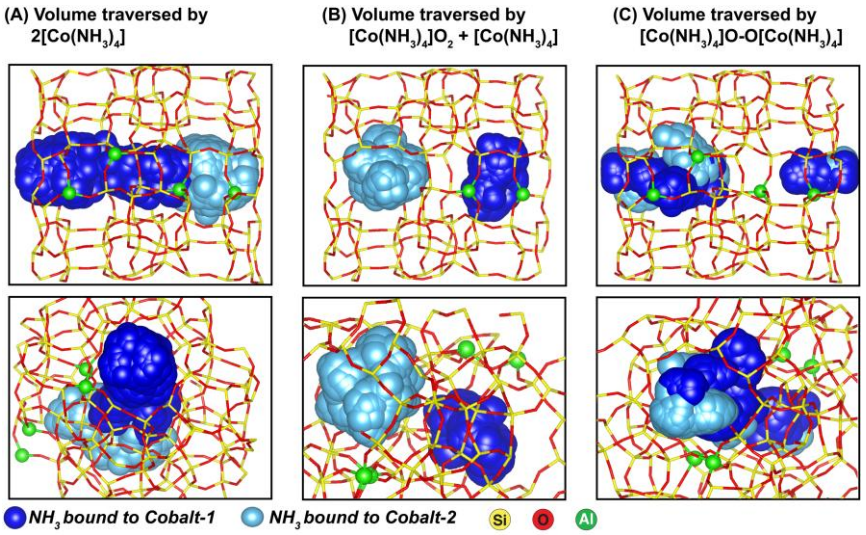

Supplementary Fig. 43. Mobility of each species during 1 ns MD simulations for the 4Al config.1. (A) $2[Co(NH_3)_4]^{2+}$, (B) $[Co(NH_3)_4\text{-}O_2]^{2+}$ + $[Co(NH_3)_4]^{2+}$, and (C) $[Co(NH_3)_4\text{-}O_2\text{-}Co(NH_3)_4]^{4+}$.

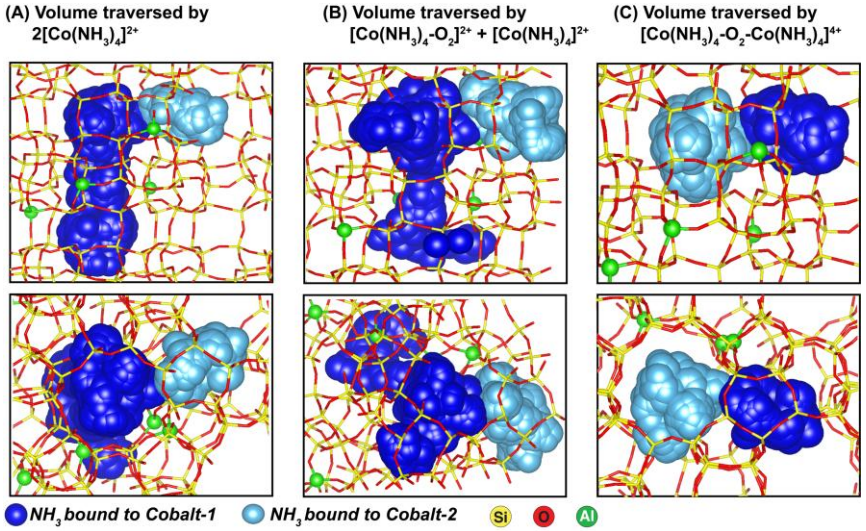

Supplementary Fig. 44. Mobility of each species during 1 ns MD simulations for the 4Al config.2. (A) $2[Co(NH_3)_4]^{2+}$, (B) $[Co(NH_3)_4\text{-}O_2]^{2+}$ + $[Co(NH_3)_4]^{2+}$, and (C) $[Co(NH_3)_4\text{-}O_2\text{-}Co(NH_3)_4]^{4+}$.

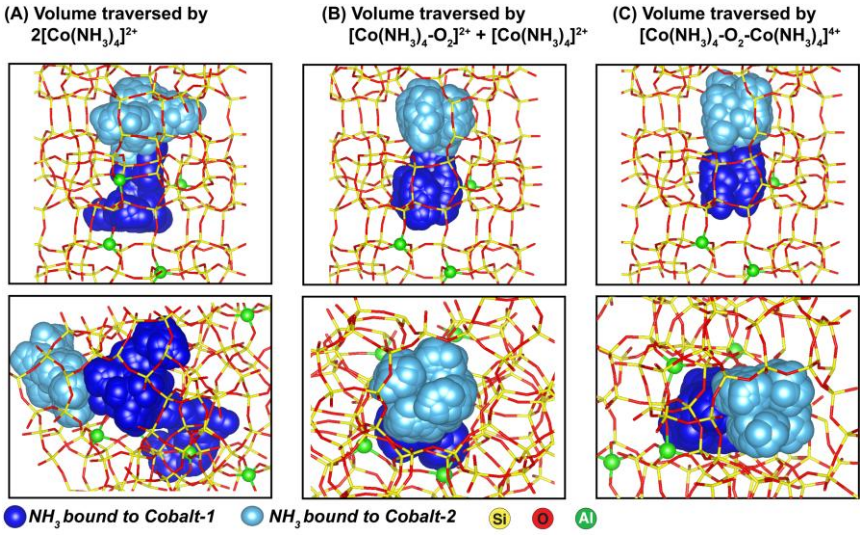

Supplementary Fig. 45. Mobility of each species during 1 ns MD simulations for the 4Al config.3. (A) $2[Co(NH_3)_4]^{2+}$, (B) $[Co(NH_3)_4\text{-}O_2]^{2+}$ + $[Co(NH_3)_4]^{2+}$, and (C) $[Co(NH_3)_4\text{-}O_2\text{-}Co(NH_3)_4]^{4+}$.

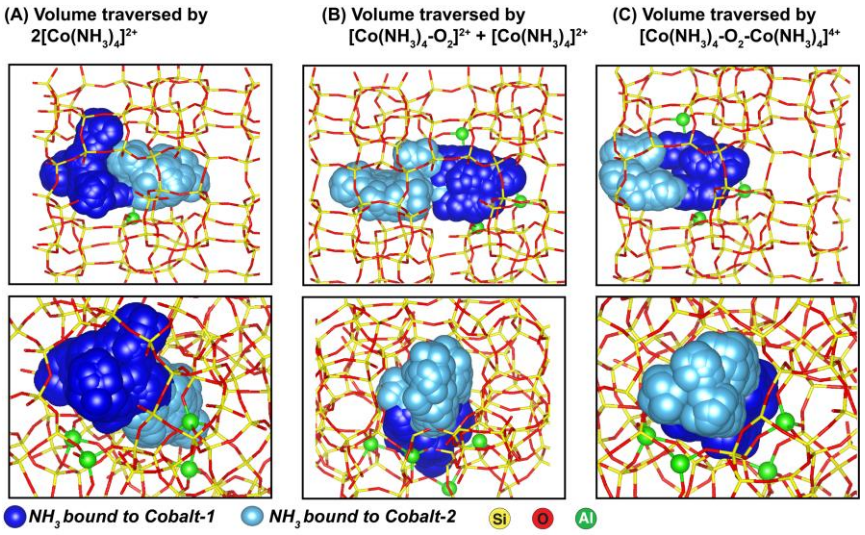

Supplementary Fig. 46. Mobility of each species during 1 ns MD simulations for the 4Al config.4. (A) $2[Co(NH_3)_4]^{2+}$, (B) $[Co(NH_3)_4\text{-}O_2]^{2+}$ + $[Co(NH_3)_4]^{2+}$, and (C) $[Co(NH_3)_4\text{-}O_2\text{-}Co(NH_3)_4]^{4+}$.

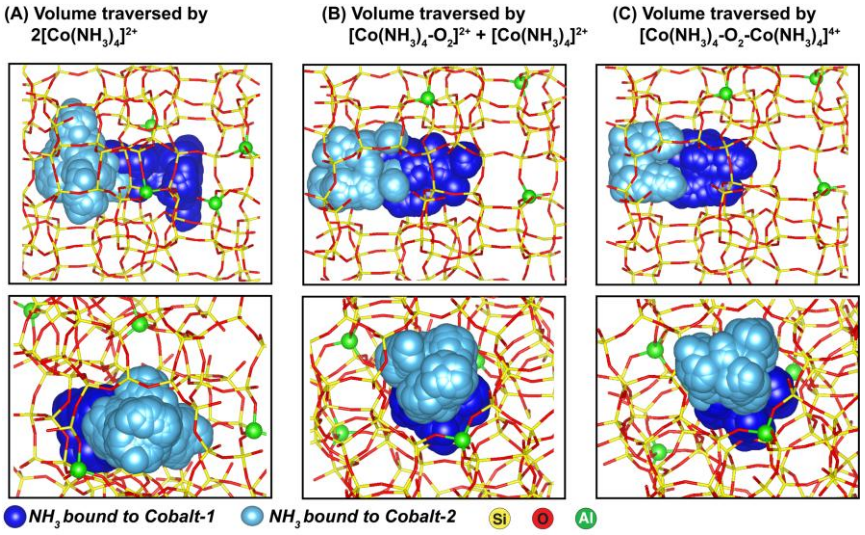

Supplementary Fig. 47. Mobility of each species during 1ns MD simulations for the 4Al config.5. (A) $2[Co(NH_3)_4]^{2+}$, (B) $[Co(NH_3)_4\text{-}O_2]^{2+}$ + $[Co(NH_3)_4]^{2+}$, and (C) $[Co(NH_3)_4\text{-}O_2\text{-}Co(NH_3)_4]^{4+}$.

Radial distribution functions of species located in 4Al configurations

We used distances obtained from 1000 equally spaced (in time) snapshots of 1 ns MD simulation for computing radial distribution function of each species. The zeolite framework atoms are neglected in radial distribution function analysis. We create bins of 0.05 Å for the atomic distances from 0-10 Å using *'ase_get_all_distances()'* function to get pairwise distances between atoms (including periodic boundary conditions). Then, frequencies in each bin were normalized such that the integral of the normalized frequency (plotted as RDF in Supplementary Figs. 48-52) over the 0-10 Å distance range is 1. For ease of visualization of the Co-O_f RDF, especially in the 2-3 Å range, the normalization was performed such that the maximum value of the Co-O_f RDF is 1.

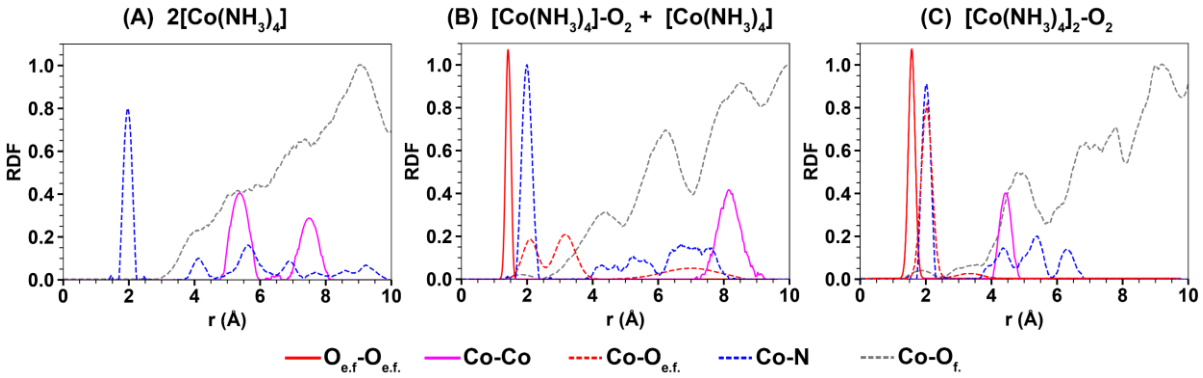

Supplementary Fig. 48. Radial distribution functions of (A) $2[Co(NH_3)_4]^{2+}$, (B) $[Co(NH_3)_4\text{-}O_2]^{2+} + [Co(NH_3)_4]^{2+}$, and (C) $[Co(NH_3)_4\text{-}O_2\text{-}Co(NH_3)_4]^{4+}$ located in 4Al configuration 1 (black, Fig. 3A, main text). Coordination to the extra framework oxygen atoms ($O_{e.f.}$) and framework oxygen atoms ($O_{f.}$) plotted separately for clarity.

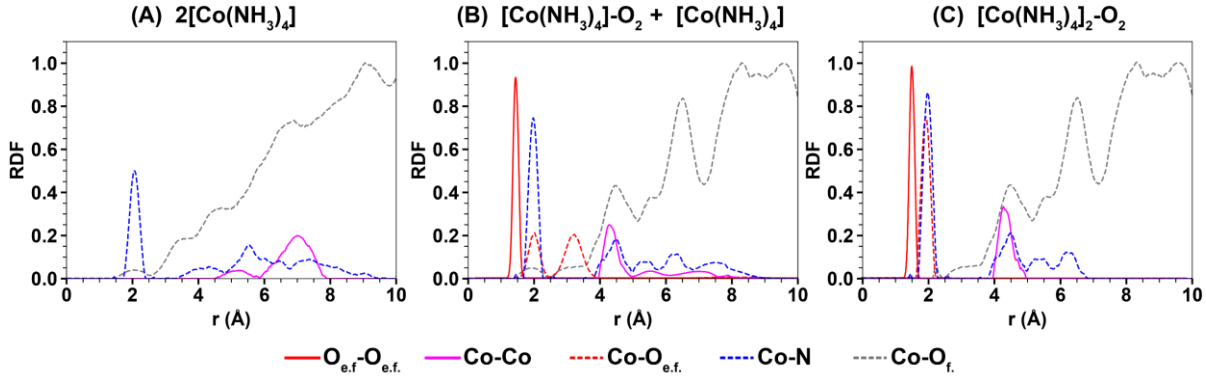

Supplementary Fig. 49. Radial distribution functions of (A) $2[Co(NH_3)_4]^{2+}$, (B) $[Co(NH_3)_4\text{-}O_2]^{2+} + [Co(NH_3)_4]^{2+}$, and (C) $[Co(NH_3)_4\text{-}O_2\text{-}Co(NH_3)_4]^{4+}$ located in 4Al configuration 2 (orange, Fig. 3A, main text). Coordination to the extra framework oxygen atoms ($O_{e.f.}$) and framework oxygen atoms ($O_{f.}$) plotted separately for clarity.

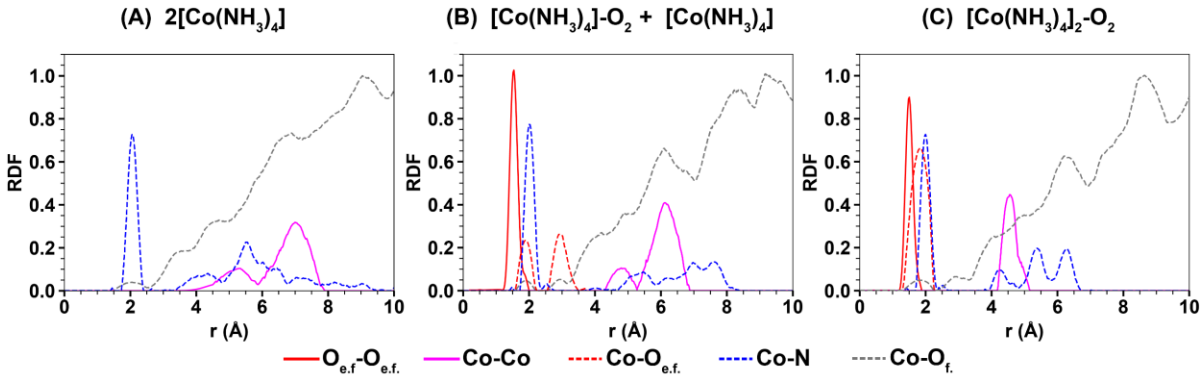

Supplementary Fig. 50. Radial distribution functions of (A) $2[Co(NH_3)_4]^{2+}$, (B) $[Co(NH_3)_4\text{-}O_2]^{2+}$ + $[Co(NH_3)_4]^{2+}$, and (C) $[Co(NH_3)_4\text{-}O_2\text{-}Co(NH_3)_4]^{4+}$ located in 4Al configuration 3 (purple, Fig. 3A, main text). Coordination to the extra framework oxygen atoms ($O_{e.f.}$) and framework oxygen atoms ($O_{f.}$) plotted separately for clarity.

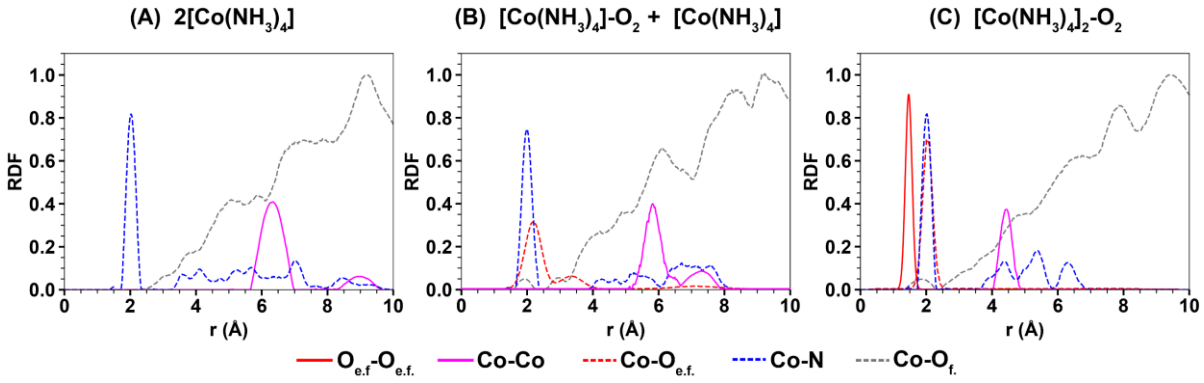

Supplementary Fig. 51. Radial distribution functions of (A) $2[Co(NH_3)_4]^{2+}$, (B) $[Co(NH_3)_4\text{-}O_2]^{2+}$ + $[Co(NH_3)_4]^{2+}$, and (C) $[Co(NH_3)_4\text{-}O_2\text{-}Co(NH_3)_4]^{4+}$ located in 4Al configuration 4 (pink, Fig. 3A, main text). Coordination to the extra framework oxygen atoms ($O_{e.f.}$) and framework oxygen atoms ($O_{f.}$) plotted separately for clarity.

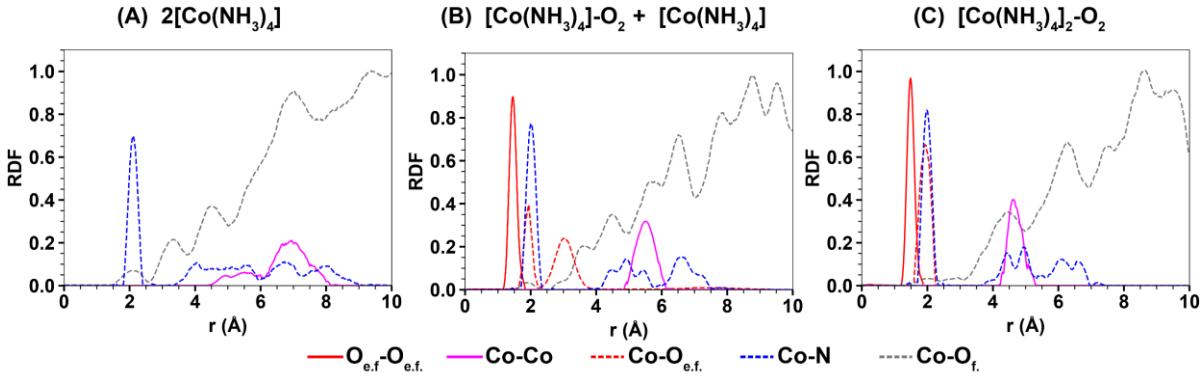

Supplementary Fig. 52. Radial distribution functions of (A) $2[Co(NH_3)_4]^{2+}$, (B) $[Co(NH_3)_4\text{-}O_2]^{2+}$ + $[Co(NH_3)_4]^{2+}$, and (C) $[Co(NH_3)_4\text{-}O_2\text{-}Co(NH_3)_4]^{4+}$ located in 4Al configuration 5 (teal, Fig. 3A, main text). Coordination to the extra framework oxygen atoms ($O_{e.f.}$) and framework oxygen atoms ($O_{f.}$) plotted separately for clarity.

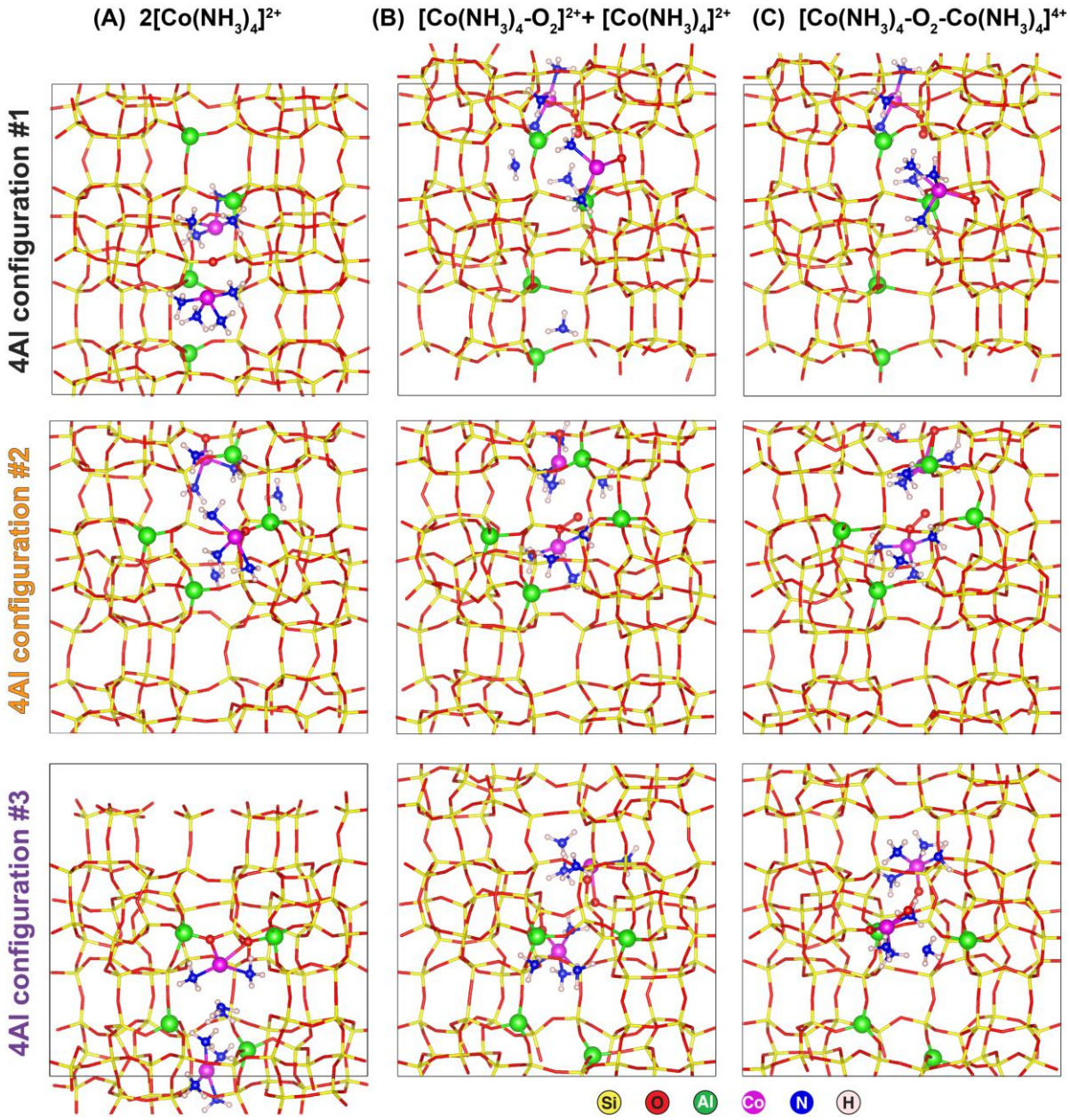

Supplementary Fig. 53. Partially framework coordinated (A) $2[Co(NH_3)_4]^{2+}$, (B) $[Co(NH_3)_4\text{-}O_2]^{2+}$ + $[Co(NH_3)_4]^{2+}$, and (C) $[Co(NH_3)_4\text{-}O_2\text{-}Co(NH_3)_4]^{4+}$ located in different 4Al configurations 1, 2 and 3 (numbers correspond to Fig. 3A, main text) in MFI. Snapshots shown are the structures with the minimum Co-O_f (extra framework oxygen) distances (not the lowest energy structures) of each species, taken from the MD simulations and the coordinating framework oxygen atoms are shown as red spheres.

Supplementary Note 6. Reaction Energies of Oxygen-containing-intermediates

DFT functional sensitivity for relative energies of oxygen containing dicobalt complexes

Supplementary Table 9. Relative energies (0 K) of $[Co(NH_3)_4\text{-}O_2\text{-}Co(NH_3)_4]^{4+}$ in gas phase and in MFI calculated using PBE-D3(BJ).

	Gas phase	4Al config 1	4Al config 2
trans-μ-1,2-peroxo dicobalt	0	0	0
μ- η2: η2 peroxo dicobalt	+27	+14	+31
bis-μ-oxo dicobalt	+154	+155	+177

Supplementary Table 10. DFT calculated relative energies of $[Co(NH_3)_4\text{-}O_2\text{-}Co(NH_3)_4]^{4+}$ in gas phase and in MFI using DFT+U (U=3.0) with PBE-D3(BJ).

	Gas phase	4Al config 1	4Al config 2
trans-μ-1,2-peroxo dicobalt	0	0	0
μ- η2: η2 peroxo dicobalt	+31	+16	+35
bis- μ-oxo dicobalt	+161	+156	+182

Supplementary Table 11. DFT calculated relative energies of $[Co(NH_3)_4\text{-}O_2\text{-}Co(NH_3)_4]^{4+}$ in gas phase and in MFI using HSE06-D3(BJ).

	Gas phase	4Al config 1	4Al config 2
trans-μ-1,2-peroxo dicobalt	0	0	0
μ- η2: η2 peroxo dicobalt	+6	+19	+38
bis- μ-oxo dicobalt	+148	+161	+160

Sensitivity of reaction energies to Al configuration

We computed the reaction energies of potential intermediates at monomeric and dimeric sites using the following reactions:

$2\ [Co(NH_3)_4]^{2+} + O_2 \rightarrow [Co(NH_3)_4\text{-}O_2\text{-}Co(NH_3)_4]^{4+}$ ***… Equation S12***

$[Co(NH_3)_4]^{2+} + O_2 \rightarrow [Co(NH_3)_4\text{-}O_2]^{2+}$ ***… Equation S13***

$[Co(NH_3)_4]^{2+} + 1/2\ O_2 \rightarrow [Co(NH_3)_4\text{-}O]^{2+}$ ***… Equation S14***

The computed reaction energies of Equations S12-S14 (PBE values are in Supplementary Table 12, other DFT functionals are in Supplementary Tables 13-14) are sensitive to the 4Al configurations but either mildly exergonic or endergonic in all cases, indicating that the formation of these reactive intermediates is thermodynamically reasonable. Notably, the dimer formation energies in the zeolite are considerably (200 – 500 kJ·mol^{-1}) lower than the dimer formation energy in the gas phase (computed in vacuum).

Supplementary Table 12. DFT calculated reaction energies at 0 K in kJ mol $^{-1}$ for gas phase (vacuum) and each of the 4Al configurations in MFI using PBE-D3(BJ).

	Gas phase	**4Al config 1**	**4Al config 2**	**4Al config 3**	**4Al config 4**	**4Al config 5**
Dimer formation (Equation S12)	+288	-107	-122	-156	-178	-170
Peroxo/Superoxo formation (Equation S13)	-76	-151	-160	-146	-156	-164
Oxo formation (Equation S14)	+76	+66	+49	+121	+19	+67

To investigate the more exothermic reaction energy caused by the presence of the zeolite, we first calculated the interaction energy between two $[Co(NH_3)_4]^{2+}$ cations placed in a vacuum using DFT. We placed the two cations in a simulation box of 50 Å × 50 Å × 50 Å to minimize periodic effects and applied a net background charge of 4+ to the system (NELECT=78). We calculated the potential energy of the system by increasing the distance between two Co centers from 5 Å to 12 Å in steps of 0.5 Å (Supplementary Fig. 54) while keeping all other degrees of freedom constant (e.g. fixed Co-N, N-H distances for a given $[Co(NH_3)_4]^{2+}$). Next, we assessed the Coulombic energy between two $[Co(NH_3)_4]^{2+}$ cations placed in a vacuum using the Coulomb equation:

$$E_{Coulomb} = \frac{k_e}{\varepsilon_r}\frac{q_{Co}\,q_{Co}}{d_{Co-Co}} \qquad \textit{… Equation S15}$$

using the constant, $k_e = \frac{1}{4\pi\varepsilon_0} = 8.988 \times 10^9\ Nm^2C^{-2}$ with free space permittivity (ε_0), distance between two Co atoms (d_{Co-Co}), and the relative permittivity (ε_r) of 1.

For MFI, we estimated the Coulomb interaction energy (Supplementary Fig. 54) using the ε_r of MFI reported in literature [32], that ranges from 1.7 to 2.6 depending on the frequency of the electrical signal used in the study. Although factors such as chemical composition, defect density, crystallite size and the presence of species such as cations and structure directing agents may change the relative permittivity, we think that this range is representative of our Co-MFI samples (and they have relatively low Co loadings). Supplementary Fig. 54A shows that MFI offers 270 – 400 kJ·mol^{-1} lower energy penalty to put two monomers at a 5 Å

separation, as needed for the formation of $[Co(NH_3)_4\text{-}O_2\text{-}Co(NH_3)_4]^{4+}$ (Supplementary Figs. 48-52, RDFs). Additionally, our DFT calculations show that the dispersion interactions among adsorbates on each Co atom (Supplementary Fig. 54B) can change the interaction by ~ 50 kJ mol^{-1}. In the MFI, dispersive interactions with zeolite framework that are dictated by the local pore environment can also change the energy penalty for keeping two $[Co^{II}(NH_3)_4]^{2+}$ in proximity. However, we expect Coulombic interactions to be the dominant interaction between two Co centers, thereby rationalizing the lower dimer formation energies we observed in MFI compared to vacuum.

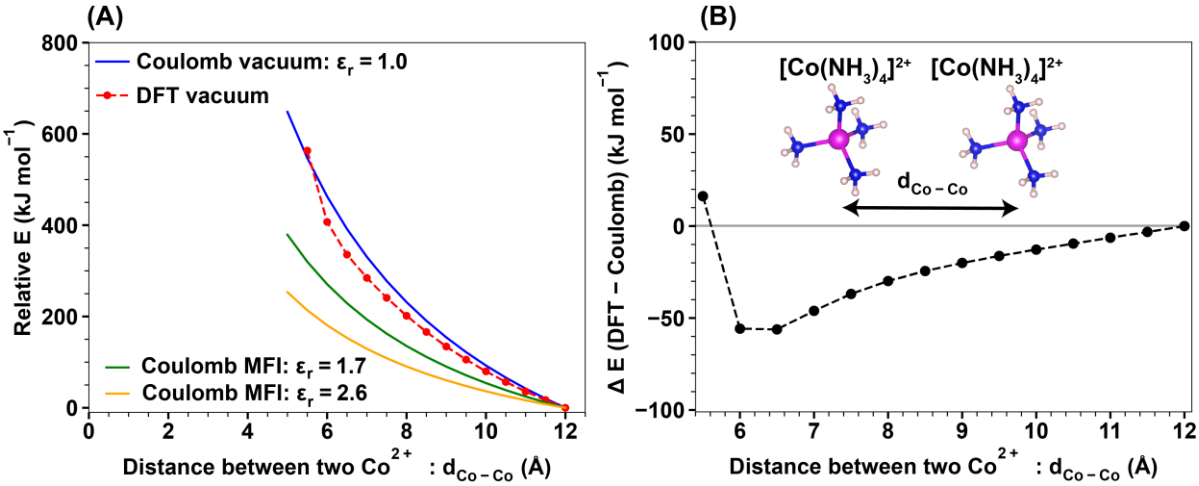

Supplementary Fig. 54. (A) Variation of the potential energy of two $[Co(NH_3)_4]^{2+}$ placed in a vacuum estimated using DFT and Coulomb's law. The Coulomb law was used with a relative permittivity of (1.7-2.5) in the zeolite (green). (B) The DFT computed energy – Coulombic energy vs the Co-Co separation distance.

Reaction energies using different DFT functionals

Supplementary Table 13. DFT calculated reaction energies at 0 K in kJ·mol^{-1} for gas phase (vacuum) and each 4Al configuration in MFI using DFT+U (U=3.0) with PBE-D3(BJ).

	Gas phase	**4Al config 1**	**4Al config 2**	**4Al config 3**	**4Al config 4**	**4Al config 5**
Dimer formation (S13)	+270	-141	-134	-196	-182	-202
Peroxo/Superoxo formation (S14)	-71	-170	-182	-174	-156	-189
Oxo formation (S15)	+69	+89	+58	+145	+14	+73

Supplementary Table 14. DFT calculated reaction energies at 0 K in kJ·mol^{-1} for gas phase (vacuum) and each 4Al configuration in MFI using HSE06-D3(BJ).

	Gas phase	**4Al config 1**	**4Al config 2**	**4Al config 3**	**4Al config 4**	**4Al config 5**
Dimer formation (S13)	+310	-99	-149	-187	-148	-190
Peroxo/Superoxo formation (S14)	-89	-121	-162	-182	-102	-193
Oxo formation (S15)	+96	+85	+49	+121	+19	+69

Reaction free energies at 648 K for different 4Al configurations in MFI

Supplementary Table 15. Estimated reaction free energies at 648 K in kJ·mol $^{-1}$ for gas phase and each 4Al configuration in MFI with the PBE-D3(BJ). Entropies of NH_3 solvated cationic species were calculated from MD simulations with their respective MLP.

	Gas phase	**4Al config 1**	**4Al config 2**	**4Al config 3**	**4Al config 4**	**4Al config 5**
Dimer formation (S13)	+432	+37	22	-19	-8	-2
Peroxo/Superoxo formation (S14)	+70	-5	-14	0	-29	-7
Oxo formation (S15)	+141	+131	+115	+184	+84	+128

Supplementary Note 7. Kinetic Measurements

We examined the kinetically relevant step for oxidative activation of C_2H_6 under the ammoxidation condition by comparing the reaction rates when substituting C_2H_6 with C_2D_6 (Supplementary Fig. 55). At 623 K, the rates of C_2H_6 consumption and product formation (CH_3CN, C_2H_4, and CO_2) decrease when introducing C_2D_6 instead of C_2H_6, exhibiting a normal kinetic isotope effect (KIE) (k_{C2H6}/k_{C2D6} = 1.78)

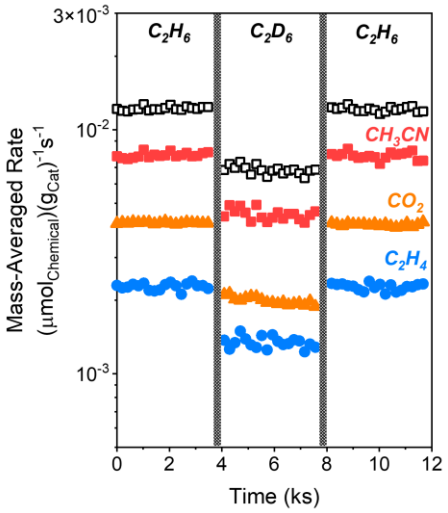

Supplementary Fig. 55. Kinetic isotope effect on mass-averaged rates of C_2H_6 consumption (□), and product formation CH_3CN (◆), C_2H_4 (●), CO_2 (▲)) over Co-ZSM-5 under ammoxidation (0.5 kPa C_2H_6 or C_2D_6, 7.5 kPa O_2, 5 kPa NH_3) condition at 648 K.

The dependence of reaction rates on reactant pressures provides insight into reaction mechanisms. Similar to the rate measurements in Supplementary Note 2, we measured rates of reactant consumption and product formation over both H-ZSM-5 and Co-ZSM-5 with two different cobalt concentrations (0.139 $mmol_{Co}{\cdot}g_{cat}^{-1}$ and 0.039 $mmol_{Co}{\cdot}g_{cat}^{-1}$) as a function of C_2H_6, O_2, and NH_3 pressures to deconvolute the reactions specifically involving Co^{II} ion sites.

Supplementary Fig. 56 shows the rates of C_2H_6 consumption and product formation (CH_3CN, C_2H_4, and CO_2) over H-ZSM-5 and Co-ZSM-5 while varying C_2H_6, O_2, NH_3, and H_2O pressures under ammoxidation conditions. The rates of C_2H_6 consumption show a nearly 1st-order dependence on C_2H_6 pressures ($r_{C2H6} \sim [C_2H_6]^{1.3}$ for H-ZSM-5; $r_{C2H6} \sim [C_2H_6]^{1}$ for Co-ZSM-5 with high cobalt concentration; $r_{C2H6} \sim [C_2H_6]^{1.3}$ for Co-ZSM-5 with low cobalt concentration), but sublinearly depend on the O_2 pressures ($r_{C2H6} \sim [O_2]^{0.2}$ for H-ZSM-5; $r_{C2H6} \sim [O_2]^{0.1}$ for Co-ZSM-5 with high cobalt concentration; $r_{C2H6} \sim [O_2]^{0.2}$ for Co-ZSM-5 with low cobalt concentration). Additionally, the reaction rates decrease with NH_3 pressures ($r_{C2H6} \sim [NH_3]^{-0.5}$ for H-ZSM-5; $r_{C2H6} \sim [NH_3]^{-0.3}$ for Co-ZSM-5 with high cobalt concentration; $r_{C2H6} \sim [NH_3]^{-0.4}$ for Co-ZSM-5 with low cobalt concentration).

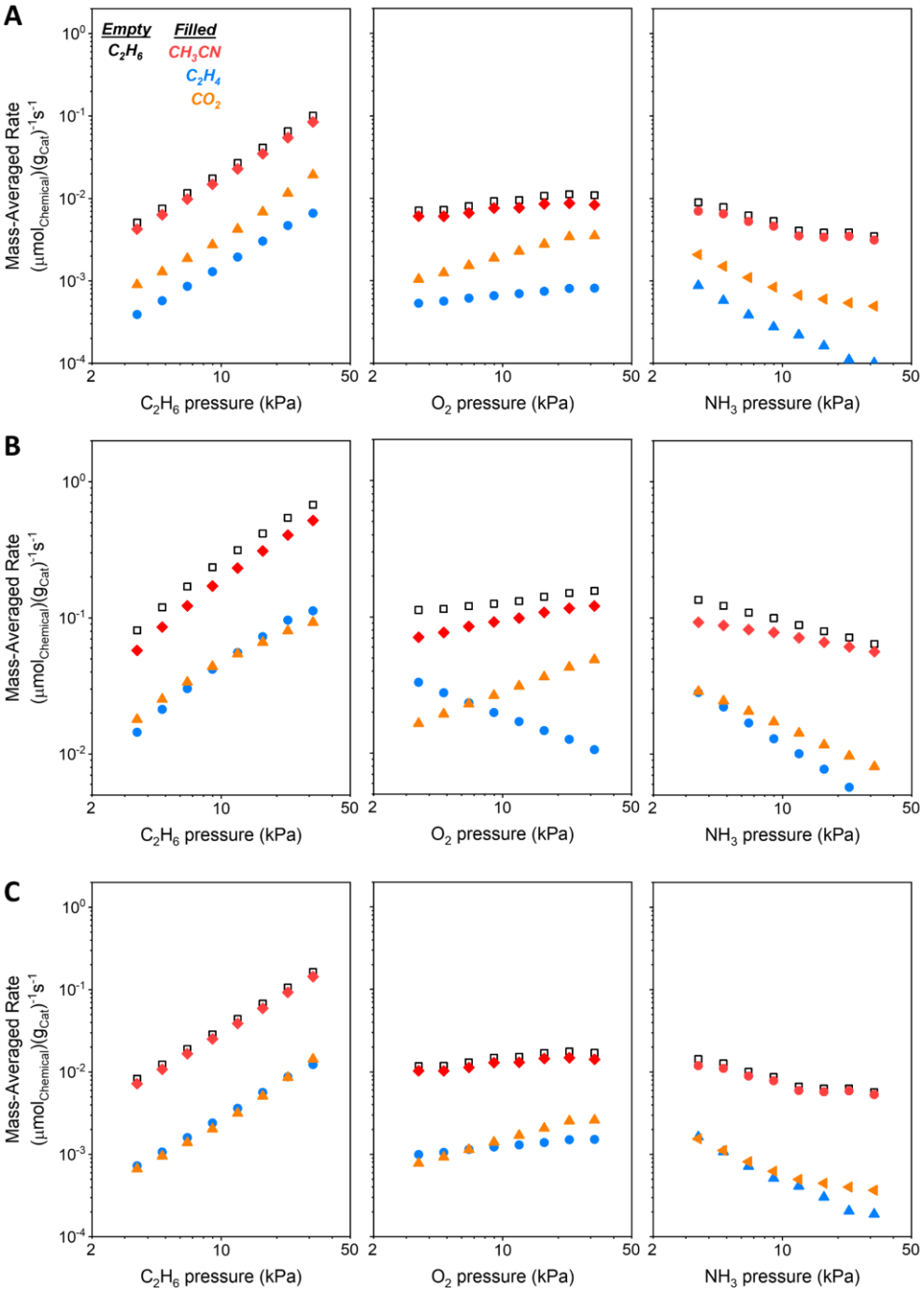

Supplementary Fig. 56. Mass averaged rates of C_2H_6 consumption (□), and product formation CH_3CN (◆), C_2H_4 (●), CO_2 (▲)) under ammoxidation conditions at 648 K as a function of C_2H_6 pressures (7.5 kPa O_2, 5 kPa NH_3), O_2 pressures (5 kPa C_2H_6, 5 kPa NH_3), and NH_3 pressures (7.5 kPa O_2, 5 kPa C_2H_6) over (A) H-ZSM-5, (B) Co-ZSM-5 (d_{Co}=0.139 $mmol_{Co}\cdot g_{cat}^{-1}$), and (C) Co-ZSM-5 ($d_{Co}$=0.039 $mmol_{Co}\cdot g_{cat}^{-1}$).

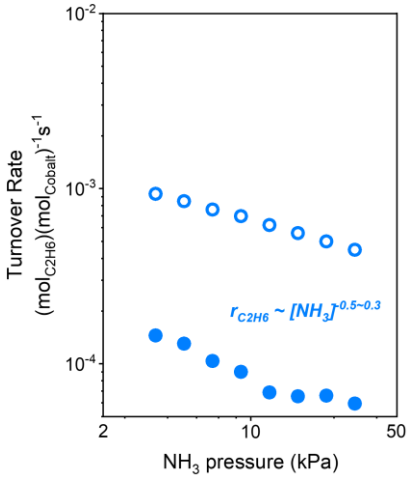

Supplementary Fig. 57. C_2H_6 consumption rates normalized by cobalt atoms on materials with either high (0.139 $mmol_{Co} \cdot g_{cat}^{-1}$, ○) or low (0.039 $mmol_{Co} \cdot g_{cat}^{-1}$, ●) cobalt concentrations as functions of NH_3 pressures (7.5 kPa O_2, 5 kPa C_2H_6) during ammoxidation at 648 K.

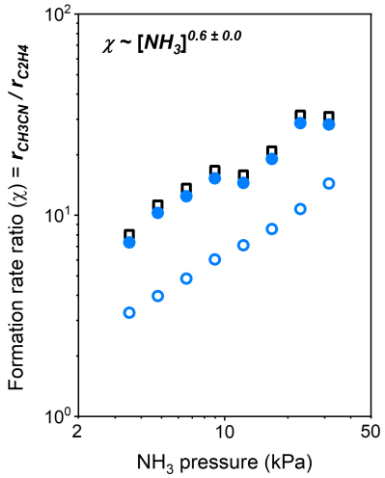

Supplementary Fig. 58. Formation rate ratios (χ) of acetonitrile to ethylene on materials with either high (0.139 $mmol_{Co} \cdot g_{cat}^{-1}$, ○) and low (0.039 $mmol_{Co} \cdot g_{cat}^{-1}$, ●) of cobalt concentrations of Co-ZSM-5 and H-ZSM-5 (□) as a function of NH_3 pressures (7.5 kPa O_2, 5 kPa C_2H_6) during ammoxidation at 648 K.

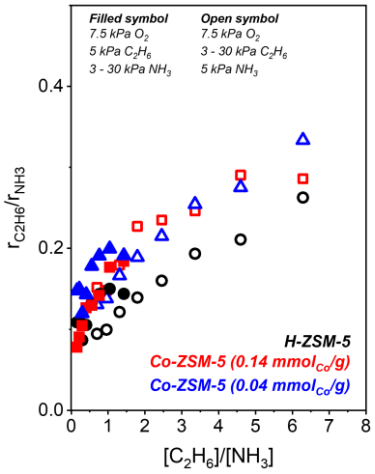

Supplementary Fig. 59. Ratios of C_2H_6 consumption rates to NH_3 consumption rates as a function of reactant pressure ratios of C_2H_6 to NH_3 during ammoxidation reactions at 648 K over H-ZSM-5, Co-ZSM-5 (d_{Co}=0.139 $mmol_{Co}\cdot g_{cat}^{-1}$), and Co-ZSM-5 ($d_{Co}$=0.039 $mmol_{Co}\cdot g_{cat}^{-1}$).

Supplementary Note 8. Derivation of Rate Expression

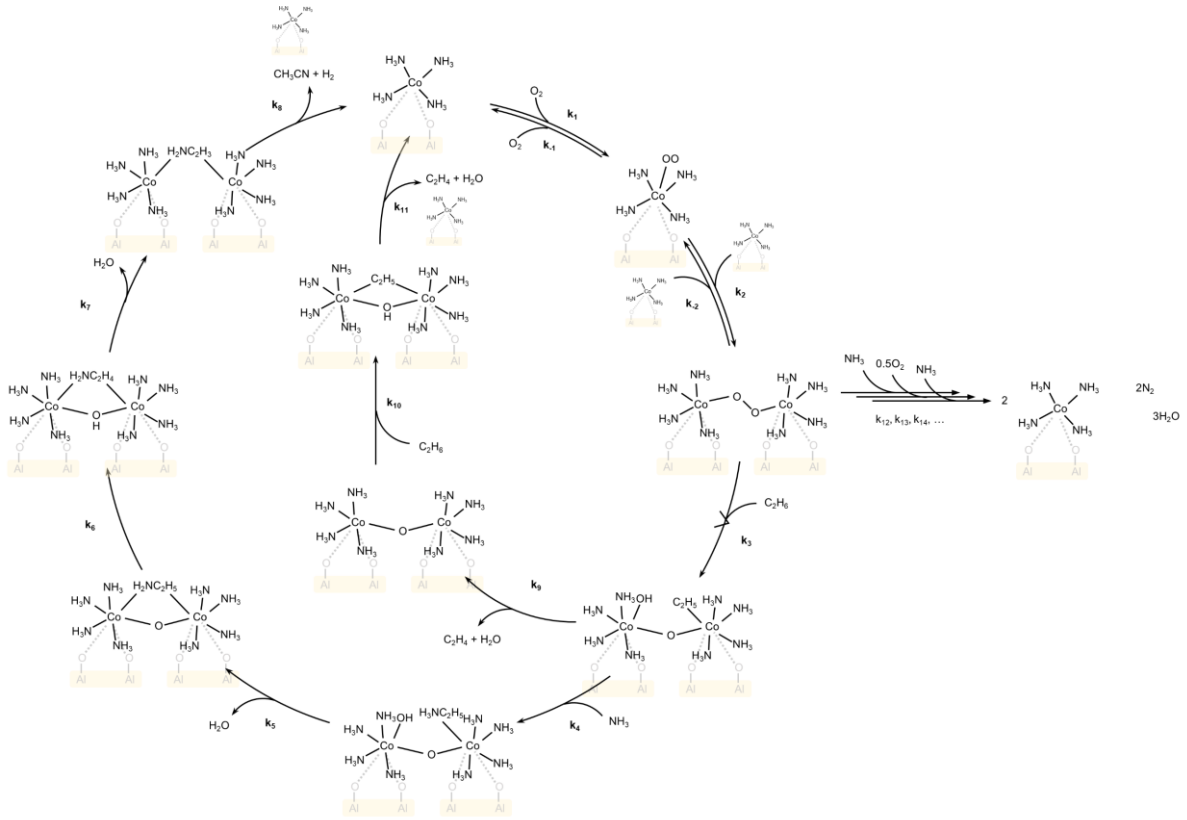

Elementary Steps for Ammoxidation

$$O_2 + Co(NH_3)_4 \underset{k_{-1}}{\overset{k_1}{\rightleftharpoons}} Co(NH_3)_4\text{-}OO \qquad \textit{...Step 1}$$

$$Co(NH_3)_4\text{-}OO + Co(NH_3)_4 \underset{k_{-2}}{\overset{k_2}{\rightleftharpoons}} Co(NH_3)_4\text{-}OO\text{-}Co(NH_3)_4 \qquad \textit{...Step 2}$$

$$C_2H_6 + Co(NH_3)_4\text{-}OO\text{-}Co(NH_3)_4 \xrightarrow{k_3} Co(NH_3)_4\text{-}OH(C_2H_5)(O)\text{-}Co(NH_3)_4 \qquad \textit{...Step 3}$$

$$NH_3 + Co(NH_3)_4\text{-}OH(C_2H_5)(O)\text{-}Co(NH_3)_4 \xrightarrow{k_4} Co(NH_3)_4\text{-}OH(C_2H_5NH_3)(O)\text{-}Co(NH_3)_4 \qquad \textit{...Step 4}$$

$$Co(NH_3)_4\text{-}OH(C_2H_5NH_3)(O)\text{-}Co(NH_3)_4 \xrightarrow{k_5} Co(NH_3)_4\text{-}C_2H_5NH_2(O)\text{-}Co(NH_3)_4 + H_2O \qquad \textit{...Step 5}$$

$$Co(NH_3)_4\text{-}C_2H_5NH_2(O)\text{-}Co(NH_3)_4 \xrightarrow{k_6} Co(NH_3)_4\text{-}C_2H_4NH_2(OH)\text{-}Co(NH_3)_4 \qquad \textit{...Step 6}$$

$$Co(NH_3)_4\text{-}C_2H_4NH_2(OH)\text{-}Co(NH_3)_4 \xrightarrow{k_7} Co(NH_3)_4\text{-}C_2H_3NH_2\text{-}Co(NH_3)_4 + H_2O \qquad \textit{...Step 7}$$

$$Co(NH_3)_4\text{-}C_2H_3NH_2\text{-}Co(NH_3)_4 \xrightarrow{k_8} 2\ Co(NH_3)_4 + CH_3CN + H_2 \qquad \textit{...Step 8}$$

$$Co(NH_3)_4\text{-}OH(C_2H_5)(O)\text{-}Co(NH_3)_4 \xrightarrow{k_9} Co(NH_3)_4\text{-}O\text{-}Co(NH_3)_4 + C_2H_4 + H_2O \qquad \textit{...Step 9}$$

$$C_2H_6 + Co(NH_3)_4\text{-}O\text{-}Co(NH_3)_4 \xrightarrow{k_{10}} Co(NH_3)_4\text{-}\ C_2H_5(OH)\text{-}Co(NH_3)_4 \qquad \textit{...Step 10}$$

$$Co(NH_3)_4\text{-}C_2H_5(OH)\text{-}Co(NH_3)_4 \xrightarrow{k_{11}} 2\ Co(NH_3)_4 + C_2H_4 + H_2O \qquad \textit{...Step 11}$$

$$2\ NH_3 + 0.5\ O_2 + Co(NH_3)_4\text{-}OO\text{-}Co(NH_3)_4 \xrightarrow{k_{12},\ k_{13},\ k_{14},\ \ldots} 2\ Co(NH_3)_4 + 2\ N_2 + 3\ H_2O \qquad \textit{...Step 12, 13, 14, ...}$$

Supplementary Scheme 2. Proposed catalytic cycle and elementary steps with surface intermediates for C_2H_6 consumption over Co-ZSM-5 under ammoxidation conditions. k_n and k_{-n} are rate constants of forward and backward reactions in step n, respectively. $\rightleftharpoons$

represents a reversible step; $\longrightarrow$ illustrates a irreversible step; and $\longrightarrow\!\!\!\!\!\!\wedge\!\!\!\!\!\!\longrightarrow$ shows a kinetically relevant step.

Under the ammoxidation conditions, the dominant cobalt species become $[Co(NH_3)_4]^{2+}$, so the reaction begins with the adsorption of O_2 on these species (step 1). As the reaction temperature is high enough to induce mobility of $[Co(NH_3)_4]^{2+}$, another $[Co(NH_3)_4]^{2+}$ reacts with $[Co(NH_3)_4\text{-}O_2]^{2+}$ to form $[Co(NH_3)_4\text{-}O_2\text{-}Co(NH_3)_4]^{4+}$ (step 2). Oxo species of this oxygen-intermediate cleaves C-H bond of C_2H_6, forming form surface-bound OH and C_2H_5 intermediates (step 3). NH_3 may introduce C-N bond to surface-bound C_2H_5 to form $C_2H_5NH_3$ (step 4), which subsequently reacts with OH to produce surface-bound $C_2H_5NH_2$ (step 5). Further reactions of surface-bound $C_2H_5NH_2$ produce CH_3CN, H_2, and H_2O (steps 6, 7, and 8). Simultaneously, the surface-bound OH and C_2H_5 intermediates may form C_2H_4 and H_2O, remaining oxo-bridged dimer (step 9). This oxo-bridged dimer also forms C_2H_4 and H_2O from C_2H_6 and closes the catalytic cycle by regenerating $[Co(NH_3)_4]^{2+}$ (steps 10 and 11). Additionally, $[Co(NH_3)_4\text{-}O_2\text{-}Co(NH_3)_4]^{4+}$ is competitively consumed by NH_3 oxidation (steps 12, 13, 14…). The elementary steps of NH_3 oxidation are still ambiguous, but steady state operation represents that each step for NH_3 oxidation have nearly identical reaction rates ($r_{12} \approx r_{13} \approx r_{14} \approx \ldots$).

Both steps 3 and 10 consume C_2H_6, so the C_2H_6 consumption rate is the sum of them.

$$r_{C_2H_6} = r_3 + r_{10} = -k_3[C_2H_6][Co(NH_3)_4 - OO - Co(NH_3)_4] - k_{10}[C_2H_6][Co(NH_3)_4 - O - Co(NH_3)_4]$$

… Equation S16

We apply pseudo-steady state hypothesis for all the surface intermediates.

$$k_{-1}[Co(NH_3)_4 - OO] + 2k_8[Co(NH_3)_4 - C_2H_3NH_2 - Co(NH_3)_4] + 2k_{11}[Co(NH_3)_4 - C_2H_5(OH) - Co(NH_3)_4] + k_{-2}[Co(NH_3)_4 - OO - Co(NH_3)_4] + 2k_{12}[NH_3][Co(NH_3)_4 - OO - Co(NH_3)_4] = k_1[O_2][Co(NH_3)_4] + k_2[Co(NH_3)_4 - OO][Co(NH_3)_4]$$

… Equation S17

$$k_1[O_2][Co(NH_3)_4] + k_{-2}[Co(NH_3)_4 - OO - Co(NH_3)_4] = k_{-1}[Co(NH_3)_4 - OO] + k_2[Co(NH_3)_4 - OO][Co(NH_3)_4]$$

… Equation 18

$$k_2[Co(NH_3)_4 - OO][Co(NH_3)_4] = k_{-2}[Co(NH_3)_4 - OO - Co(NH_3)_4] + k_3[C_2H_6][Co(NH_3)_4 - OO - Co(NH_3)_4] + k_{12}[NH_3][Co(NH_3)_4 - OO - Co(NH_3)_4]$$

… Equation S19

$$k_3[C_2H_6][Co(NH_3)_4 - OO - Co(NH_3)_4] = k_4[NH_3][Co(NH_3)_4 - OH(C_2H_5)(O) - Co(NH_3)_4] + k_9[Co(NH_3)_4 - OH(C_2H_5)(O) - Co(NH_3)_4]$$

… Equation S20

$$k_4[NH_3][Co(NH_3)_4 - OH(C_2H_5)(O) - Co(NH_3)_4] = k_5[Co(NH_3)_4 - OH(C_2H_5NH_3)(O) - Co(NH_3)_4]$$

… Equation S21

$$k_5[Co(NH_3)_4 - OH(C_2H_5NH_3)(O) - Co(NH_3)_4] = k_6[Co(NH_3)_4 - C_2H_5NH_2(O) - Co(NH_3)_4]$$

… Equation S22

$$k_6[Co(NH_3)_4 - C_2H_5NH_2(O) - Co(NH_3)_4] = k_7[Co(NH_3)_4 - C_2H_4NH_2(OH) - Co(NH_3)_4]$$

… Equation S23

$$k_7[Co(NH_3)_4 - C_2H_4NH_2(OH) - Co(NH_3)_4] = k_8[Co(NH_3)_4 - C_2H_3NH_2 - Co(NH_3)_4]$$

… Equation S24

$$k_9[Co(NH_3)_4 - OH(C_2H_5)(O) - Co(NH_3)_4] = k_{10}[C_2H_6][Co(NH_3)_4 - O - Co(NH_3)_4]$$

… Equation S25

$$k_{10}[C_2H_6][Co(NH_3)_4 - O - Co(NH_3)_4] = k_{11}[Co(NH_3)_4 - C_2H_5(OH) - Co(NH_3)_4]$$

… Equation S26

The total cobalt sites ([L]) are sum of cobalt-ammine complexes and all the surface-bound intermediates.

$$\begin{aligned}[L] = {} & [Co(NH_3)_4] + [Co(NH_3)_4 - OO] + [Co(NH_3)_4 - OO - Co(NH_3)_4] \\ & + [Co(NH_3)_4 - OH(C_2H_5)(O) - Co(NH_3)_4] \\ & + [Co(NH_3)_4 - OH(C_2H_5NH_3)(O) - Co(NH_3)_4] \\ & + [Co(NH_3)_4 - C_2H_5NH_2(O) - Co(NH_3)_4] \\ & + [Co(NH_3)_4 - C_2H_4NH_2(OH) - Co(NH_3)_4] \\ & + [Co(NH_3)_4 - C_2H_3NH_2 - Co(NH_3)_4] + [Co(NH_3)_4 - O - Co(NH_3)_4] \\ & + [Co(NH_3)_4 - C_2H_5(OH) - Co(NH_3)_4] + \cdots\end{aligned}$$

… Equation S27

The concentrations of surface intermediates can be replaced by $[Co(NH_3)_4]$, $[O_2]$, $[C_2H_6]$, and $[NH_3]$ using Equations S17 – S26.

$$\begin{aligned}[L] = [Co(NH_3)_4] & + \frac{k_1(k_{-2} + k_3[C_2H_6] + k_{12}[NH_3])}{k_2(k_3[C_2H_6] + k_{12}[NH_3])[Co(NH_3)_4] + k_{-1}(k_{-2} + k_3[C_2H_6] + k_{12}[NH_3])}[O_2][Co(NH_3)_4] \\ & + \frac{k_1k_2}{k_2(k_3[C_2H_6] + k_{12}[NH_3])[Co(NH_3)_4] + k_{-1}(k_{-2} + k_3[C_2H_6] + k_{12}[NH_3])}[O_2][Co(NH_3)_4]^2 \\ & + \frac{k_1k_2k_3}{(k_4[NH_3] + k_9)(k_2(k_3[C_2H_6] + k_{12}[NH_3])[Co(NH_3)_4] + k_{-1}(k_{-2} + k_3[C_2H_6] + k_{12}[NH_3]))}[O_2][C_2H_6][Co(NH_3)_4]^2 \\ & + \frac{k_1k_2k_3k_4}{k_5(k_4[NH_3] + k_9)(k_2(k_3[C_2H_6] + k_{12}[NH_3])[Co(NH_3)_4] + k_{-1}(k_{-2} + k_3[C_2H_6] + k_{12}[NH_3]))}[O_2][C_2H_6][NH_3][Co(NH_3)_4]^2 \\ & + \frac{k_1k_2k_3k_4}{k_6(k_4[NH_3] + k_9)(k_2(k_3[C_2H_6] + k_{12}[NH_3])[Co(NH_3)_4] + k_{-1}(k_{-2} + k_3[C_2H_6] + k_{12}[NH_3]))}[O_2][C_2H_6][NH_3][Co(NH_3)_4]^2 \\ & + \frac{k_1k_2k_3k_4}{k_7(k_4[NH_3] + k_9)(k_2(k_3[C_2H_6] + k_{12}[NH_3])[Co(NH_3)_4] + k_{-1}(k_{-2} + k_3[C_2H_6] + k_{12}[NH_3]))}[O_2][C_2H_6][NH_3][Co(NH_3)_4]^2 \\ & + \frac{k_1k_2k_3k_4}{k_8(k_4[NH_3] + k_9)(k_2(k_3[C_2H_6] + k_{12}[NH_3])[Co(NH_3)_4] + k_{-1}(k_{-2} + k_3[C_2H_6] + k_{12}[NH_3]))}[O_2][C_2H_6][NH_3][Co(NH_3)_4]^2 \\ & + \frac{k_1k_2k_3k_9}{k_{10}(k_4[NH_3] + k_9)(k_2(k_3[C_2H_6] + k_{12}[NH_3])[Co(NH_3)_4] + k_{-1}(k_{-2} + k_3[C_2H_6] + k_{12}[NH_3]))}[O_2][Co(NH_3)_4]^2 \\ & + \frac{k_1k_2k_3k_9}{k_{11}(k_4[NH_3] + k_9)(k_2(k_3[C_2H_6] + k_{12}[NH_3])[Co(NH_3)_4] + k_{-1}(k_{-2} + k_3[C_2H_6] + k_{12}[NH_3]))}[O_2][C_2H_6][Co(NH_3)_4]^2 + \cdots\end{aligned}$$

… Equation S28

The rate expression for C_2H_6 consumption rate normalized by the total cobalt sites becomes the following.

$$\frac{r_{C_2H_6}}{[L]} = -\frac{\frac{k_1k_2k_3}{(k_2(k_3[C_2H_6] + k_{12}[NH_3])[Co(NH_3)_4] + k_{-1}(k_{-2} + k_3[C_2H_6] + k_{12}[NH_3]))}\left(\frac{k_4[NH_3] + 2k_9}{k_4[NH_3] + k_9}\right)[O_2][C_2H_6][Co(NH_3)_4]^2}{[L]}$$

… Equation S29

This can be simplified by grouping the terms with A, B, and C.

$$\frac{r_{C_2H_6}}{[L]} = -\frac{\frac{A}{B[Co(NH_3)_4] + C}[O_2][C_2H_6][Co(NH_3)_4]^2}{[L]}$$

… Equation S30

$$A = k_1 k_2 k_3 \left(\frac{k_4[NH_3]+2k_9}{k_4[NH_3]+k_9}\right) \quad \textit{… Equation S31}$$

$$B = k_2(k_3[C_2H_6] + k_{12}[NH_3]) \quad \textit{… Equation S32}$$

$$C = k_{-1}(k_{-2} + k_3[C_2H_6] + k_{12}[NH_3]) \quad \textit{… Equation S33}$$

This rate expression shows inverse dependence of C_2H_6 consumption rates on NH_3 pressures due to competitive consumption of $[Co(NH_3)_4\text{-}O_2\text{-}Co(NH_3)_4]^{4+}$, as displayed in Supplementary Fig. 57. However, we may consider the reaction conditions when $[NH_3]$ is given as a constant. Additionally, since NH_3 consumption rates are generally faster than C_2H_6 consumptions rates, $k_{12}[NH_3]$ is comparably larger than others (k_{-2} and $k_3[C_2H_6]$) (Supplementary Fig. 58). These make A, B, and C being considered as constants.

Finally, we considered three cases with different types of the most abundant reaction intermediate (MARI) that potentially lead to the rate expression in accordance with the experimental results: (1) $[Co(NH_3)_4]^{2+}$ MARI, (2) $[Co(NH_3)_4\text{-}O_2]^{2+}$ MARI, and (3) $[Co(NH_3)_4]^{2+}$ and $[Co(NH_3)_4\text{-}O_2]^{2+}$ mixed MARI. It is because other MARIs never derive the first-order dependence of C_2H_6 consumption rates on C_2H_6 pressures.

(1) $[Co(NH_3)_4]^{2+}$ MARI

This assumption indicates $[L] \approx [Co(NH_3)_4]$. If we further assume $k_{12}[NH_3]$ is comparably larger than others (k_{-2} and $k_3[C_2H_6]$), this leads to $\frac{r_{C_2H_6}}{[L]}$ in the following.

$$\frac{r_{C_2H_6}}{[L]} = -\frac{\frac{k_1k_2k_3}{(k_2(k_3[C_2H_6]+k_{12}[NH_3])[Co(NH_3)_4]+k_{-1}(k_{-2}+k_3[C_2H_6]+k_{12}[NH_3]))}\left(\frac{k_4[NH_3]+2k_9}{k_4[NH_3]+k_9}\right)[O_2][C_2H_6][Co(NH_3)_4]^2}{[L]}$$

$$= -\frac{\frac{k_1k_2k_3}{(k_2(k_{12}[NH_3])[L]+k_{-1}(k_{12}[NH_3]))}\left(\frac{k_4[NH_3]+2k_9}{k_4[NH_3]+k_9}\right)[O_2][C_2H_6][L]^2}{[L]}$$

$$= -\frac{k_1k_2k_3}{k_{12}[NH_3]}\left(\frac{k_4[NH_3]+2k_9}{k_4[NH_3]+k_9}\right)[O_2][C_2H_6]\frac{[L]}{k_2[L]+k_{-1}}$$

… Equation S34

However, this model has 1st-order dependence on $[O_2]$ and $[C_2H_6]$, and sublinear dependence on and the cobalt concentration [L]. This is not aligned with the experimental results.

(2) $[Co(NH_3)_4\text{-}O_2]^{2+}$ MARI

$$[L] \approx [Co(NH_3)_4 - OO] = \frac{k_1(k_{-2}+k_3[C_2H_6]+k_{12}[NH_3])}{k_2(k_3[C_2H_6]+k_{12}[NH_3])[Co(NH_3)_4]+k_{-1}(k_{-2}+k_3[C_2H_6]+k_{12}[NH_3])}[O_2][Co(NH_3)_4] \quad \textit{… Equation S35}$$

Using this equation, $[Co(NH_3)_4]^{2+}$ can be substituted to [L].

$$[Co(NH_3)_4] = \frac{k_{-1}(k_{-2}+k_3[C_2H_6]+k_{12}[NH_3])[L]}{k_1(k_{-2}+k_3[C_2H_6]+k_{12}[NH_3])[O_2]-k_2(k_3[C_2H_6]+k_{12}[NH_3])[L]}$$

… Equation S36

We assume $k_{12}[NH_3]$ is comparably larger than others (k_{-2} and $k_3[C_2H_6]$).

$$[Co(NH_3)_4] \approx \frac{k_{-1}[L]}{k_1[O_2]-k_2[L]} \quad \textbf{\textit{… Equation S37}}$$

On the other hand, $\frac{r_{C_2H_6}}{[L]}$ becomes as in the following.

$$\frac{r_{C_2H_6}}{[L]} = -\frac{\frac{k_1k_2k_3}{(k_2(k_3[C_2H_6]+k_{12}[NH_3])[Co(NH_3)_4]+k_{-1}(k_{-2}+k_3[C_2H_6]+k_{12}[NH_3]))}\left(\frac{k_4[NH_3]+2k_9}{k_4[NH_3]+k_9}\right)[O_2][C_2H_6][Co(NH_3)_4]^2}{[L]}$$
$$= -\frac{\frac{k_1k_2k_3}{(k_2(k_3[C_2H_6]+k_{12}[NH_3])[Co(NH_3)_4]+k_{-1}(k_{-2}+k_3[C_2H_6]+k_{12}[NH_3]))}\left(\frac{k_4[NH_3]+2k_9}{k_4[NH_3]+k_9}\right)[O_2][C_2H_6][Co(NH_3)_4]^2}{\frac{k_1(k_{-2}+k_3[C_2H_6]+k_{12}[NH_3])}{k_2(k_3[C_2H_6]+k_{12}[NH_3])[Co(NH_3)_4]+k_{-1}(k_{-2}+k_3[C_2H_6]+k_{12}[NH_3])}[O_2][Co(NH_3)_4]}$$
$$= -\frac{k_2k_3\left(\frac{k_4[NH_3]+2k_9}{k_4[NH_3]+k_9}\right)[C_2H_6][Co(NH_3)_4]}{k_{-2}+k_3[C_2H_6]+k_{12}[NH_3]}$$

… Equation S38

With assumption that $k_{12}[NH_3]$ is comparably larger than others (k_{-2} and $k_3[C_2H_6]$).

$$\frac{r_{C_2H_6}}{[L]} = -\frac{k_2k_3\left(\frac{k_4[NH_3]+2k_9}{k_4[NH_3]+k_9}\right)[C_2H_6][Co(NH_3)_4]}{k_{-2}+k_3[C_2H_6]+k_{12}[NH_3]} \approx -\frac{k_2k_3}{k_{12}[NH_3]}\left(\frac{k_4[NH_3]+2k_9}{k_4[NH_3]+k_9}\right)[C_2H_6][Co(NH_3)_4]$$

… Equation S39

By replacing $[Co(NH_3)_4]$ to [L] using Equation S37,

$$\frac{r_{C_2H_6}}{[L]} = -\frac{k_2k_3}{k_{12}[NH_3]}\left(\frac{k_4[NH_3]+2k_9}{k_4[NH_3]+k_9}\right)[C_2H_6]\frac{k_{-1}[L]}{k_1[O_2]-k_2[L]}$$

… Equation S40

This model has 1st-order dependence on $[C_2H_6]$, but inverse dependence on $[O_2]$, while the cobalt concentration [L] can be 1st-order when $k_1[O_2] >> k_2[L]$. Despite uncertainty of the order of [L], the inverse dependence on $[O_2]$ does not match the experimental observation.

(3) $[Co(NH_3)_4]^{2+}$ and $[Co(NH_3)_4\text{-}O_2]^{2+}$ mixed MARI

$$[L] \approx [Co(NH_3)_4] + [Co(NH_3)_4 - OO] \quad = [Co(NH_3)_4] + \frac{k_1(k_{-2}+k_3[C_2H_6]+k_{12}[NH_3])}{k_2(k_3[C_2H_6]+k_{12}[NH_3])[Co(NH_3)_4]+k_{-1}(k_{-2}+k_3[C_2H_6]+k_{12}[NH_3])}[O_2][Co(NH_3)_4]$$

… Equation S41

To express $[Co(NH_3)_4]^{2+}$ in terms of [L]

$$[Co(NH_3)_4] = \frac{\left([L]k_2(k_3[C_2H_6]+k_{12}[NH_3])-\left(\frac{k_1}{k_{-1}}[O_2]+1\right)k_{-1}(k_{-2}+k_3[C_2H_6]+k_{12}[NH_3])\right)+\sqrt{\left(k_2(k_3[C_2H_6]+k_{12}[NH_3])[L]-\left(\frac{k_1}{k_{-1}}[O_2]+1\right)k_{-1}(k_{-2}+k_3[C_2H_6]+k_{12}[NH_3])\right)^2+4k_2(k_3[C_2H_6]+k_{12}[NH_3])k_{-1}(k_{-2}+k_3[C_2H_6]+k_{12}[NH_3])[L]}}{2k_2(k_3[C_2H_6]+k_{12}[NH_3])}$$

… Equation S42

With assumptions that $k_{12}[NH_3]$ is comparably larger than others (k_{-2} and $k_3[C_2H_6]$).

$$[Co(NH_3)_4] = \frac{(k_2[L]-(k_1[O_2]+k_{-1}))+\sqrt{\left(k_2[L]-(k_1[O_2]+k_{-1})\right)^2+4k_2k_{-1}[L]}}{2k_2}$$

… Equation S43

$$\frac{r_{C_2H_6}}{[L]} = -\frac{\frac{k_1k_2k_3}{(k_2(k_3[C_2H_6]+k_{12}[NH_3])[Co(NH_3)_4]+k_{-1}(k_{-2}+k_3[C_2H_6]+k_{12}[NH_3]))}\left(\frac{k_4[NH_3]+2k_9}{k_4[NH_3]+k_9}\right)[O_2][C_2H_6][Co(NH_3)_4]^2}{[L]}$$

$$= -\frac{\frac{k_1k_2k_3}{(k_2(k_3[C_2H_6]+k_{12}[NH_3])[Co(NH_3)_4]+k_{-1}(k_{-2}+k_3[C_2H_6]+k_{12}[NH_3]))}\left(\frac{k_4[NH_3]+2k_9}{k_4[NH_3]+k_9}\right)[O_2][C_2H_6][Co(NH_3)_4]^2}{[Co(NH_3)_4]+\frac{k_1(k_{-2}+k_3[C_2H_6]+k_{12}[NH_3])}{k_2(k_3[C_2H_6]+k_{12}[NH_3])[Co(NH_3)_4]+k_{-1}(k_{-2}+k_3[C_2H_6]+k_{12}[NH_3])}[O_2][Co(NH_3)_4]}$$

$$= -\frac{\frac{k_1k_2k_3}{(k_2(k_3[C_2H_6]+k_{12}[NH_3])[Co(NH_3)_4]+k_{-1}(k_{-2}+k_3[C_2H_6]+k_{12}[NH_3]))}\left(\frac{k_4[NH_3]+2k_9}{k_4[NH_3]+k_9}\right)[O_2][C_2H_6][Co(NH_3)_4]}{1+\frac{k_1(k_{-2}+k_3[C_2H_6]+k_{12}[NH_3])}{k_2(k_3[C_2H_6]+k_{12}[NH_3])[Co(NH_3)_4]+k_{-1}(k_{-2}+k_3[C_2H_6]+k_{12}[NH_3])}[O_2]}$$

… Equation S44

Again, with the assumption that $k_{12}[NH_3]$ is comparably larger than others (k_{-2} and $k_3[C_2H_6]$),

$$\frac{r_{C_2H_6}}{[L]}$$

$$\approx -\frac{\frac{k_1k_2k_3}{(k_2(k_{12}[NH_3])[Co(NH_3)_4]+k_{-1}k_{12}[NH_3])}\left(\frac{k_4[NH_3]+2k_9}{k_4[NH_3]+k_9}\right)[O_2][C_2H_6][Co(NH_3)_4]}{1+\frac{k_1k_{12}[NH_3]}{k_2(k_{12}[NH_3])[Co(NH_3)_4]+k_{-1}k_{12}[NH_3]}[O_2]}$$

$$\approx -\frac{\frac{k_1k_2k_3}{k_{12}[NH_3]}\left(\frac{k_4[NH_3]+2k_9}{k_4[NH_3]+k_9}\right)[O_2][C_2H_6][Co(NH_3)_4]}{k_2[Co(NH_3)_4]+k_{-1}+k_1[O_2]}$$

… Equation S45

Finally, $[Co(NH_3)_4]^{2+}$ is replaced with [L] from Equation S43.

$$\frac{r_{C_2H_6}}{[L]} = -\frac{k_1k_2k_3}{k_{12}[NH_3]}\left(\frac{k_4[NH_3]+2k_9}{k_4[NH_3]+k_9}\right)[O_2][C_2H_6]\frac{(k_2[L]-(k_1[O_2]+k_{-1}))+\sqrt{(k_2[L]-(k_1[O_2]+k_{-1}))^2+4k_2k_{-1}[L]}}{2k_2\left(k_2\frac{(k_2[L]-(k_1[O_2]+k_{-1}))+\sqrt{(k_2[L]-(k_1[O_2]+k_{-1}))^2+4k_2k_{-1}[L]}}{2k_2}+k_{-1}+k_1[O_2]\right)}$$

… Equation S46

Since the rate equation is still complicated, we further examine this equation in three different cases depending on the values of $k_2[L]$ and $(k_1[O_2] + k_{-1})$.

(3-1) $k_2[L] >> k_1[O_2] + k_{-1}$

In this case, Equation S43 can be simplified as

$$[Co(NH_3)_4] = \frac{(k_2[L]-(k_1[O_2]+k_{-1}))+\sqrt{(k_2[L]-(k_1[O_2]+k_{-1}))^2+4k_2k_{-1}[L]}}{2k_2}$$

$$\approx [L]$$

… Equation S47

The rate in Equation S46 becomes

$$\frac{r_{C_2H_6}}{[L]} \approx -\frac{k_1k_2k_3}{k_{12}[NH_3]}\left(\frac{k_4[NH_3]+2k_9}{k_4[NH_3]+k_9}\right)[O_2][C_2H_6]\frac{[L]}{(k_2[L]+k_{-1}+k_1[O_2])}$$

$$\approx -\frac{k_1k_3}{k_{12}[NH_3]}\left(\frac{k_4[NH_3]+2k_9}{k_4[NH_3]+k_9}\right)[O_2][C_2H_6]$$

… Equation S48

This rate expression gives the 1st-order and 0th-order dependences on $[O_2]$ and cobalt concentration, respectively, which does not explain the experimental observations.

(3-2) $k_2[L] \sim k_1[O_2] + k_{-1}$

In this case, we assume $k_2[L] \approx (k_1[O_2] + k_{-1})$, leading to the following equation from Equation S43.

$$[Co(NH_3)_4] = \frac{\left(k_2[L] - (k_1[O_2] + k_{-1})\right) + \sqrt{\left(k_2[L] - (k_1[O_2] + k_{-1})\right)^2 + 4k_2k_{-1}[L]}}{2k_2} \approx \sqrt{\frac{k_{-1}}{k_2}[L]}$$

… Equation S49

The rate in Equation S46 becomes

$$\frac{r_{C_2H_6}}{[L]} \approx -\frac{k_1k_2k_3}{k_{12}[NH_3]}\left(\frac{k_4[NH_3] + 2k_9}{k_4[NH_3] + k_9}\right)[O_2][C_2H_6]\frac{\sqrt{\frac{k_{-1}}{k_2}[L]}}{\left(\sqrt{k_2k_{-1}[L]} + k_{-1} + k_1[O_2]\right)}$$

… Equation S50

This model has 1st-order dependence on the $[C_2H_6]$, and sublinear dependence on $[O_2]$, which corresponds to the experimental observations. However, [L] determines the reaction rates sublinearly with the reaction order at maximum of 0.5th-order, which deviates from the experimental observation (1st-order)

(3-3) $k_2[L] << k_1[O_2] + k_{-1}$

In this case, using binomial expansion ($\sqrt{1+x} = 1 + \frac{1}{2}x - \frac{1}{8}x^2 + \cdots, when\ x \ll 1$), Equation S43 can be simplified as

$$[Co(NH_3)_4] = \frac{\left(k_2[L] - (k_1[O_2] + k_{-1})\right) + \sqrt{\left(k_2[L] - (k_1[O_2] + k_{-1})\right)^2 + 4k_2k_{-1}[L]}}{2k_2} \approx \frac{k_{-1}[L]}{k_1[O_2] + k_{-1}}$$

… Equation S51

The rate in Equation S46 becomes

$$\frac{r_{C_2H_6}}{[L]} \approx -\frac{k_1k_2k_3}{k_{12}[NH_3]}\left(\frac{k_4[NH_3] + 2k_9}{k_4[NH_3] + k_9}\right)[O_2][C_2H_6]\frac{\frac{k_{-1}[L]}{k_1[O_2] + k_{-1}}}{\left(k_2\frac{k_{-1}[L]}{k_1[O_2] + k_{-1}} + k_{-1} + k_1[O_2]\right)}$$

$$= -\frac{k_1 k_2 k_3}{k_{12}[NH_3]}\left(\frac{k_4[NH_3]+2k_9}{k_4[NH_3]+k_9}\right)[O_2][C_2H_6]\frac{k_{-1}[L]}{k_2 k_{-1}[L]+(k_{-1}+k_1[O_2])^2}$$

$$\approx -\frac{k_1 k_{-1} k_2 k_3}{k_{12}[NH_3]}\left(\frac{k_4[NH_3]+2k_9}{k_4[NH_3]+k_9}\right)[C_2H_6]\frac{[O_2]}{(k_{-1}+k_1[O_2])^2}[L]$$

… Equation S52

This model has 1st-order dependence on both cobalt concentration [L] and $[C_2H_6]$, and depends as a rational function on $[O_2]$. This rational function has different order depending on $k_1[O_2]/k_{-1}$.

Region	**Reaction order $[O_2]$ in $\frac{[O_2]}{(k_{-1}+k_1[O_2])^2}$**
$k_1[O_2] >> k_{-1}$	~ -1
$k_1[O_2] \sim k_{-1}$	1 ~ -1 (0 when $k_1[O_2] \approx k_{-1}$)
$k_1[O_2] << k_{-1}$	~ 1

Assuming a mixed MARI between $[Co(NH_3)_4]$ and $[Co(NH_3)_4\text{-}O_2]$, a reversible step 1 infers comparable rates for forward and backward reaction in step 1 ($k_1[O_2] \sim k_{-1}$), leading to an $[O_2]$ reaction order close to 0th. This is consistent with the experimentally observed value of 0.1.

Other Supplementary Materials

Data S1 includes DFT optimized MFI structures coordinated to zeolite lattice, H_2O, NH_3 or O_2 for 2Al and 4Al configurations (82 files), structure files used for MLP training (19 files), Raman spectra calculations: structure files, and vibrational mode visualizations (29 files), and sample code for MLP training (1 file)

References

[1] J. Guo, T. Sours, S. Holton, C. Sun, A.R. Kulkarni, Screening Cu-Zeolites for Methane Activation Using Curriculum-Based Training, ACS Catalysis, 14 (2024) 1232-1242.
[2] G. Gupta, B.C. Bukowski, Kinetic Consequences of Quasi-Harmonic Entropies Calculated with Machine Learning Interatomic Potentials for Microkinetic Modeling, The Journal of Physical Chemistry C, 128 (2024) 20104-20117.
[3] C.T. Nimlos, A.J. Hoffman, Y.G. Hur, B.J. Lee, J.R. Di Iorio, D.D. Hibbitts, R. Gounder, Experimental and Theoretical Assessments of Aluminum Proximity in MFI Zeolites and Its Alteration by Organic and Inorganic Structure-Directing Agents, Chemistry of Materials, 32 (2020) 9277-9298.
[4] D.T. Bregante, L.N. Wilcox, C. Liu, C. Paolucci, R. Gounder, D.W. Flaherty, Dioxygen Activation Kinetics over Distinct Cu Site Types in Cu-Chabazite Zeolites, ACS Catalysis, 11 (2021) 11873-11884.
[5] M.J. Frisch, G.W. Trucks, H.B. Schlegel, G.E. Scuseria, M.A. Robb, J.R. Cheeseman, G. Scalmani, V. Barone, G.A. Petersson, H. Nakatsuji, X. Li, M. Caricato, A.V. Marenich, J. Bloino, B.G. Janesko, R. Gomperts, B. Mennucci, H.P. Hratchian, J.V. Ortiz, A.F. Izmaylov, J.L. Sonnenberg, Williams, F. Ding, F. Lipparini, F. Egidi, J. Goings, B. Peng, A. Petrone, T. Henderson, D. Ranasinghe, V.G. Zakrzewski, J. Gao, N. Rega, G. Zheng, W. Liang, M. Hada, M. Ehara, K. Toyota, R. Fukuda, J. Hasegawa, M. Ishida, T. Nakajima, Y. Honda, O. Kitao, H. Nakai, T. Vreven, K. Throssell, J.A. Montgomery Jr., J.E. Peralta, F. Ogliaro, M.J. Bearpark, J.J. Heyd, E.N. Brothers, K.N. Kudin, V.N. Staroverov, T.A. Keith, R. Kobayashi, J. Normand, K. Raghavachari, A.P. Rendell, J.C. Burant, S.S. Iyengar, J. Tomasi, M. Cossi, J.M. Millam, M. Klene, C. Adamo, R. Cammi, J.W. Ochterski, R.L. Martin, K. Morokuma, O. Farkas, J.B. Foresman, D.J. Fox, Gaussian 16 Rev. C.01, Wallingford, CT, 2016.
[6] J.P. Perdew, K. Burke, M. Ernzerhof, Generalized Gradient Approximation Made Simple, Physical Review Letters, 77 (1996) 3865-3868.
[7] A.D. Becke, A new mixing of Hartree–Fock and local density-functional theories, The Journal of Chemical Physics, 98 (1993) 1372-1377.
[8] Y. Zhao, D.G. Truhlar, The M06 suite of density functionals for main group thermochemistry, thermochemical kinetics, noncovalent interactions, excited states, and transition elements: two new functionals and systematic testing of four M06-class functionals and 12 other functionals, Theoretical Chemistry Accounts, 120 (2008) 215-241.
[9] S. Grimme, S. Ehrlich, L. Goerigk, Effect of the damping function in dispersion corrected density functional theory, Journal of Computational Chemistry, 32 (2011) 1456-1465.
[10] S. Grimme, J. Antony, S. Ehrlich, H. Krieg, A consistent and accurate ab initio parametrization of density functional dispersion correction (DFT-D) for the 94 elements H-Pu, The Journal of Chemical Physics, 132 (2010).
[11] R.D.I. Johnson, NIST Computational Chemistry Comparison and Benchmark Database, Release 22, May 2022 ed., National Institute of Standards and Technology, Gaithersburg, MD, 2022.
[12] J.B. Gordon, A.C. Vilbert, M.A. Siegler, K.M. Lancaster, P. Moënne-Loccoz, D.P. Goldberg, A Nonheme Thiolate-Ligated Cobalt Superoxo Complex: Synthesis and Spectroscopic Characterization, Computational Studies, and Hydrogen Atom Abstraction Reactivity, Journal of the American Chemical Society, 141 (2019) 3641-3653.
[13] J.R. Di Iorio, R. Gounder, Controlling the Isolation and Pairing of Aluminum in Chabazite Zeolites Using Mixtures of Organic and Inorganic Structure-Directing Agents, Chemistry of Materials, 28 (2016) 2236-2247.

[14] J. Dědeček, Z. Sobalík, B. Wichterlová, Siting and Distribution of Framework Aluminium Atoms in Silicon-Rich Zeolites and Impact on Catalysis, Catalysis Reviews, 54 (2012) 135-223.
[15] X. Wang, H. Chen, W.M.H. Sachtler, Selective reduction of NOx with hydrocarbons over Co/MFI prepared by sublimation of CoBr2 and other methods, Applied Catalysis B: Environmental, 29 (2001) 47-60.
[16] W. Li, S.Y. Yu, G.D. Meitzner, E. Iglesia, Structure and Properties of Cobalt-Exchanged H-ZSM5 Catalysts for Dehydrogenation and Dehydrocyclization of Alkanes, The Journal of Physical Chemistry B, 105 (2001) 1176-1184.
[17] C. Chupin, A.C. van Veen, M. Konduru, J. Després, C. Mirodatos, Identity and location of active species for NO reduction by CH4 over Co-ZSM-5, Journal of Catalysis, 241 (2006) 103-114.
[18] Y. Li, J.N. Armor, Ammoxidation of Ethane to Acetonitrile over Metal–Zeolite Catalysts, Journal of Catalysis, 173 (1998) 511-518.
[19] G.L. Miessler, P.J. Fischer, D.A. Tarr, Inorganic Chemistry, Pearson Education2013.
[20] L. Marchese, G. Martra, N. Damilano, S. Coluccia, J.M. Thomas, Elucidating the nature of the cobalt centres in CoAPO-18 acid catalysts, Studies in Surface Science and Catalysis, 101 (1996) 861-870.
[21] J. Dědeček, L. Čapek, D. Kaucký, Z. Sobalík, B. Wichterlová, Siting and Distribution of the Co Ions in Beta Zeolite: A UV–Vis–NIR and FTIR Study, Journal of Catalysis, 211 (2002) 198-207.
[22] R.A. Schoonheydt, J. Pelgrims, Spectroscopy of cobalt–ethylenediamine–oxygen adducts in the supercages of zeolites, Journal of the Chemical Society, Dalton Transactions, (1981) 914-922.
[23] G. Lehmann, Interstitial incorporation of di- and trivalent cobalt in quartz, Journal of Physics and Chemistry of Solids, 30 (1969) 395-399.
[24] A.A. Verberckmoes, B.M. Weckhuysen, R.A. Schoonheydt, Spectroscopy and coordination chemistry of cobalt in molecular sieves1Dedicated to Professor Lovat V.C. Rees in recognition and appreciation of his lifelong devotion to zeolite science and his outstanding achievements in this field.1, Microporous and Mesoporous Materials, 22 (1998) 165-178.
[25] A.S. Hoffman, O. Müller, J. Hong, G.A. Canning, C.-Y. Fang, J.E. Perez-Aguilar, B.C. Gates, S.R. Bare, Observations of Ethylene-for-CO Ligand Exchanges on a Zeolite-Supported Single-Site Rh Catalyst by X-ray Absorption Spectroscopy, The Journal of Physical Chemistry Letters, 14 (2023) 4591-4599.
[26] B. Ravel, M. Newville, ATHENA, ARTEMIS, HEPHAESTUS: data analysis for X-ray absorption spectroscopy using IFEFFIT, Journal of Synchrotron Radiation, 12 (2005) 537-541.
[27] M.W. Chase, C.A. Davies, J.R. Downey, D.J. Frurip, R.A. McDonald, A.N. Syverud, NIST-JANAF Thermochemical Tables, 4th ed. ed., National Institute of Standards and Technology, Gaithersburg, MD, 1998.
[28] Y. Xie, J. Vandermause, L. Sun, A. Cepellotti, B. Kozinsky, Bayesian force fields from active learning for simulation of inter-dimensional transformation of stanene, npj Computational Materials, 7 (2021) 40.
[29] J. Vandermause, S.B. Torrisi, S. Batzner, Y. Xie, L. Sun, A.M. Kolpak, B. Kozinsky, On-the-fly active learning of interpretable Bayesian force fields for atomistic rare events, npj Computational Materials, 6 (2020) 20.
[30] I. Andricioaei, M. Karplus, On the calculation of entropy from covariance matrices of the atomic fluctuations, The Journal of Chemical Physics, 115 (2001) 6289-6292.

[31] A. Okuniewski, D. Rosiak, J. Chojnacki, B. Becker, Coordination polymers and molecular structures among complexes of mercury(II) halides with selected 1-benzoylthioureas, Polyhedron, 90 (2015) 47-57.
[32] M. Sun, W. Maichen, R. Pophale, Y. Liu, R. Cai, C.M. Lew, H. Hunt, M.W. Deem, M.E. Davis, Y. Yan, Dielectric constant measurement of zeolite powders by time-domain reflectometry, Microporous and Mesoporous Materials, 123 (2009) 10-14.